Geophysical Journal International

Geophys. J. Int. (2013) **193,** 1608–1626
Advance Access publication 2013 March 08

doi: 10.1093/gji/ggt058

Joint inversion of seismic and geodetic data for the source of the 2010 March 4, M_w 6.3 Jia-Shian, SW Taiwan, earthquake

Mong-Han Huang,[1] Douglas Dreger,[1] Roland Bürgmann,[1] Seung-Hoon Yoo[1] and Manabu Hashimoto[2]

[1] *Berkeley Seismological Laboratory, University of California, Berkeley, CA, USA. E-mail: mong@berkeley.edu*
[2] *Disaster Prevention Research Institute, Kyoto University, Kyoto, Japan*

Accepted 2013 February 8. Received 2013 February 6; in original form 2012 August 16

SUMMARY

The 2010 March 4, Jia-Shian (M_w 6.3) earthquake in SW Taiwan caused moderate damage and no surface rupture was observed, reflecting a deep source that is relatively rare in western Taiwan. We develop finite-source models using a combination of seismic waveform (strong motion and broadband), Global Positioning System (GPS) and synthetic aperture radar interferometry (InSAR) data to understand the rupture process and slip distribution of this event. The rupture centroid source depth is 19 km based on a series of moment tensor solution tests with improved 1-D Green's functions. The preferred fault model strikes 322° and dips 27° to the NE and the mainshock is a thrust event with a small left-lateral component. The finite-source model shows a primary slip asperity that is about 20 km in diameter at a depth range from 22 to 13 km, with peak slip of 42.5 cm, a total scalar seismic moment of 3.25×10^{18} N m (M_w 6.34) and with an average static stress drop of 0.24 MPa. The rupture velocity of this event is faster than the mid-crustal shear wave velocity in Taiwan, which suggests the possibility of a supershear event which has not been previously observed in Taiwan. Systematic resolution and sensitivity tests are performed to confirm the slip distribution, rupture velocity, the choice of weighting and smoothing for the joint inversions, and the consistency of the slip distribution. The first 24 hours of aftershocks appeared along the upper periphery of the main coseismic slip asperity. Both the mainshock and aftershocks are located in a transition zone where the depth of seismicity and an inferred regional basal décollement increases from central to southern Taiwan. The difference between the current orientation of plate convergence in Taiwan (120°) and the *P* axis of this event (052°) and nearby measurements of recent crustal strain directions (050° to 080°), as well as the relatively low static stress drop, suggest that the Jia-Shian event involves the reactivation of a deep and weak pre-existing NW–SE geological structure.

Key words: Radar interferometry; Earthquake source observations; Seismicity and tectonics; Dynamics: seismotectonics; Crustal structure.

GJI Seismology

Downloaded from http://gji.oxfordjournals.org/ at University of California, Berkeley on August 15, 2013

1 INTRODUCTION

The current tectonic framework of Taiwan is the result of the oblique collision of the Eurasian Plate and the Philippine Sea Plate. The Philippine Sea Plate moves toward the northwest with respect to Eurasia at 8.2 cm yr^{-1} (Yu *et al.* 1997; Lin *et al.* 2010), and this oblique collision has resulted in a series of N-S trending fold-and-thrust belts in the western Taiwan Foothills (Fig. 1b). In SW Taiwan, a Plio-Pleistocene foreland basin developed in response to lithospheric flexure due to the tectonic loading of the Central Range orogenic belt (Lin & Watts 2002), resulting in a geographic boundary separating the internally deforming Western Foothills and Central Range in the NE from the Pingtung Plain to the SW (Fig. 1) (Lacombe *et al.* 2001; Ching *et al.* 2011). Deffontaines *et al.* (1997) proposed that the Chishan Transfer Fault Zone (CTFZ) following this boundary (Fig. 1a) represents a NW–SE trending structural and kinematic transition zone resulting from oblique plate collision. The fold-and-thrust belt in western Taiwan has been interpreted to follow a thin-skinned model, that is, a thin, deforming wedge above a low angle detachment fault (Suppe 1981) or as a thick-skinned system where earthquakes and faults reach deep into crustal basement rocks (Wu *et al.* 1997).

The 2010 March 4, Jia-Shian (M_w 6.3) earthquake occurred in southwestern Taiwan near the SE end of the CTFZ and caused moderate damage. Ground fractures are found near Meinong (Fig. 1b for location), but there is no direct evidence that the observed surface deformations are related to the fault plane, which implies an unusually deep source. The focal depth reported by the Central Weather Bureau (CWB) is about 23 km, below the proposed basal detachment of the fold and thrust belt of Taiwan (Ching *et al.* 2011). The

© The Authors 2013. Published by Oxford University Press on behalf of The Royal Astronomical Society.

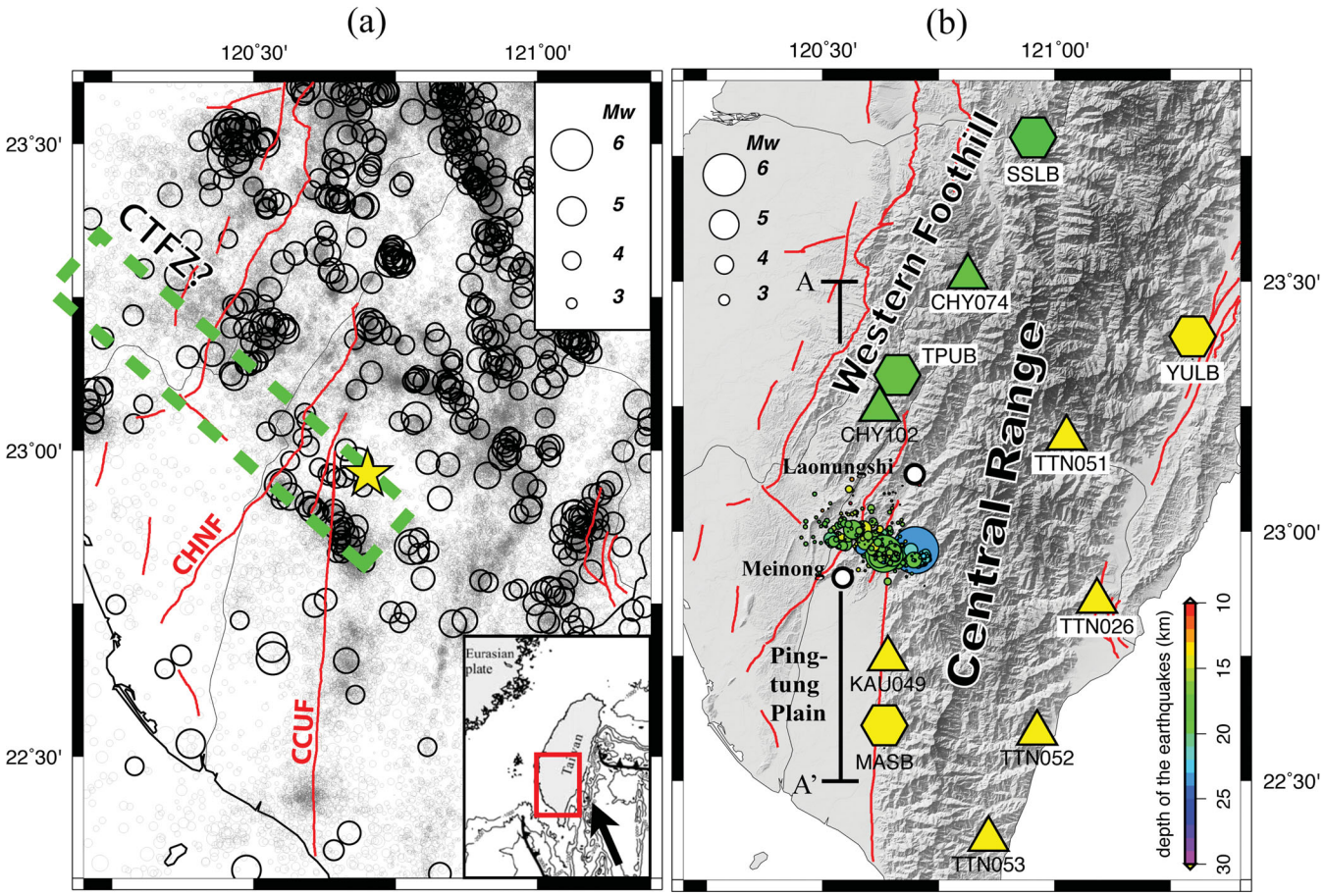

Figure 1. (a) Background seismicity of Taiwan from 1990 to 2010 (data from Wu *et al.* 2009). Earthquakes smaller and larger than *M* 3 are shown as grey and black circles, respectively. The red lines are the active faults (data from Central Geological Survey of Taiwan) and the dashed green rectangle is the inferred CTFZ (Deffontaines *et al.* 1997). The star indicates the Jia-Shian main shock. (b) Selected strong motion stations (triangles) and broadband stations (hexagons). Data from the green and yellow stations are modeled using velocity models for west and east Taiwan, respectively. The Jia-Shian main shock and aftershocks are colour coded with depth. AA′ is seismic profile for Fig. 16.

coseismic GPS measurements (Hsu *et al.* 2011) show a fan shaped pattern with azimuths from SW to NW (Fig. 2a). The greatest horizontal displacement observed with GPS is 37 mm towards N80°W and was measured about 20 km to the west of the epicentre. There are several published models for this event (e.g. Ching *et al.* 2011; Hsu *et al.* 2011; Lee *et al.* 2012), which propose a north-dipping rupture with peak fault slip of 12–35 cm based on GPS or GPS and seismic inversions.

Joint inversion techniques for kinematic earthquake models have been developed, since about two decades ago (e.g. Yoshida & Koketsu 1990; Wald & Heaton 1994; Wald & Somerville 1995; Wald *et al.* 1996; Kim & Dreger 2008). These methods combine the available seismic and geodetic data (e.g. GPS and InSAR) for an event into a joint inversion for both temporal and spatial slip variations. Generally, only the seismic data can provide information about the time history of slip, whereas the geodetic data are more sensitive to the fault geometry and the finite slip pattern. Combining both seismic and geodetic data sets allows us not only to obtain a more reliable solution but also to improve understanding of the complexity of an event. In this study, we invert for finite-source models using geodetic (GPS and InSAR) and seismic waveform (strong motion and broad-band stations) data independently and jointly, in order to compare the sensitivities of each data set and the proper smoothing parameters and data weighting for a joint inversion. We examine the rupture velocity with refined Green's functions obtained by fitting the largest Jia-Shian aftershock using the method suggested by Cohee & Beroza (1994). In addition, we also perform station sensitivity and synthetic data resolution tests to explore the reliability of the inversions.

The aim of this study is to thoroughly investigate the source characteristics of the Jia-Shian earthquake by applying the joint inversion technique, and to explore the implications for the regional seismo-tectonic environment of south Taiwan from this event. The result of the joint inversion is then put into the context of the regional geology, paleo-stress measurements and the background seismicity in order to gain further insight into the tectonic setting of the Jia-Shian event.

2 SEISMIC AND GEODETIC DATA

The Jia-Shian earthquake was recorded by two network systems operated in Taiwan, the Taiwan Strong-Motion Instrumentation Program (TSMIP) operated by the CWB of Taiwan and the Broad-band Array in Taiwan for Seismology (BATS) operated by the Institute of Earth Sciences (IES), Academia Sinica of Taiwan and CWB. More than 700 TSMIP stations and more than 20 BATS stations recorded this event. In order to avoid complex three-component wave propagation problems we select stations located within 100 km of the epicentre. In order to minimize the amplification effects when waves

Downloaded from http://gji.oxfordjournals.org/ at University of California, Berkeley on A 13

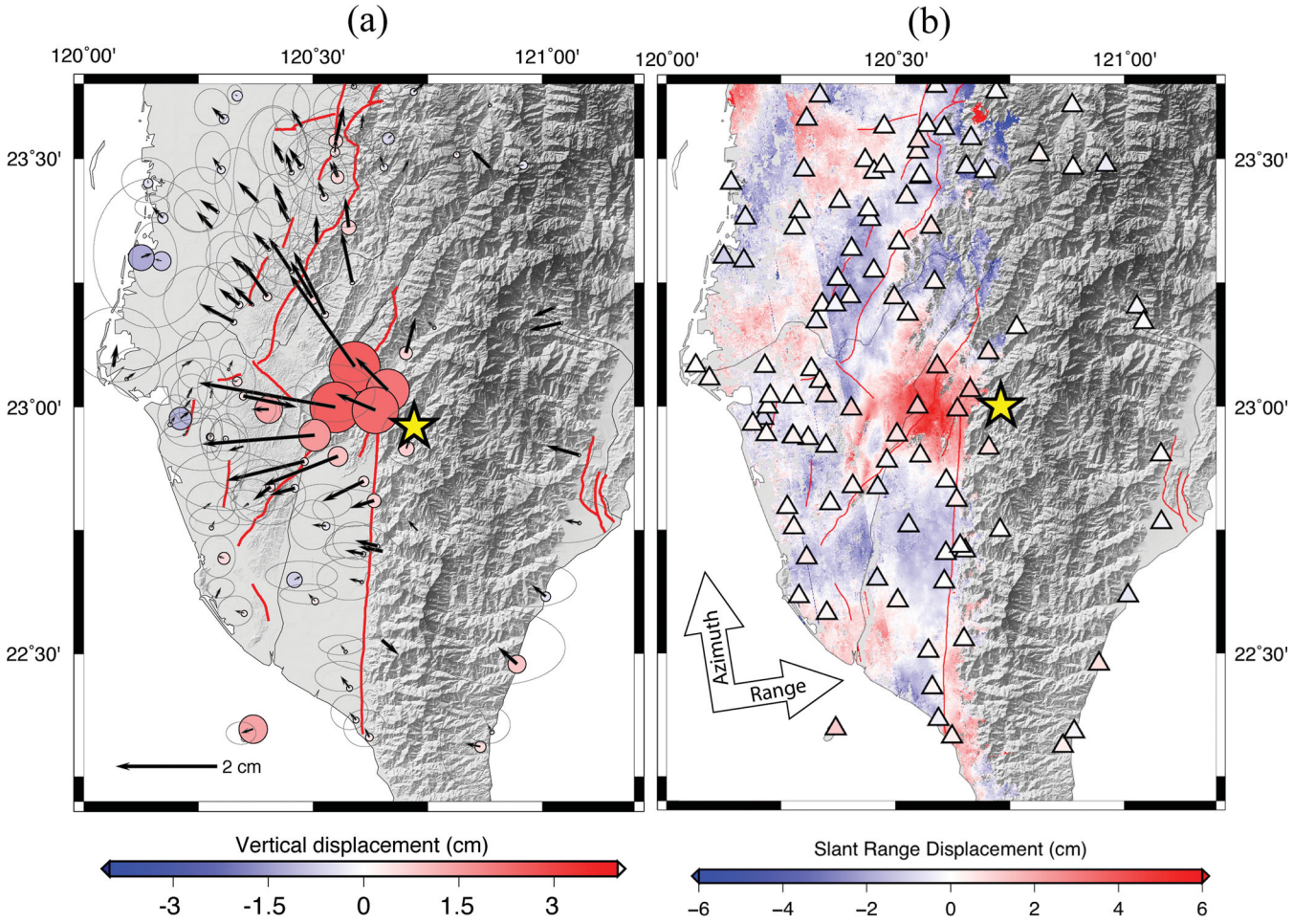

Figure 2. (a) The GPS coseismic measurements in southern Taiwan. The black arrows show the horizontal displacements with 95 per cent confidence ellipses, and the colour of the circles around the stations indicate vertical displacement. The size of the circles is scaled with the magnitude of vertical displacement. (b) ALOS coseismic interferograms. Tracks 447 and 446 are both plotted in this map. The colours represent the coseismic SRD, and the triangles are the GPS estimated SRD. Note that the GPS estimated SRD and the InSAR range changes are shown with the same colour scale.

travel through sedimentary basins, we only select seismic stations located on bedrock, while maintaining good azimuthal coverage (7 TSMIP stations and 3 BATS stations, locations see Fig. 1b). The three-component TSMIP stations record acceleration in horizontal and vertical directions with sample rates of 200 samples per second. We removed the mean offset of the seismograms and integrated twice from acceleration to displacement. Each BATS station records the velocity in east, north and vertical directions with a sample rate of 10 samples per second. We removed the instrument response and the mean offset, and integrated once from velocity to displacement. All of the seismograms are bandpass filtered between 0.03 and 0.3 Hz with a two-pole acausal Butterworth filter before resampling the data to 10 samples per second.

There are more than 350 continuous GPS (CGPS) stations deployed in Taiwan by different institutions (Yu *et al.* 2003). Most of the stations are maintained by IES of the Academia Sinica of Taiwan and data are downloadable from their website (http://gps.earth.sinica.edu.tw). The choice of CGPS stations used in our inversion is adopted from Hsu *et al.* (2011), including data from 108 CGPS stations located within a radial distance of about 80 km from the epicentre of the Jia-Shian earthquake (Fig. 2a). The data were processed with the Bernese software v.4.2 to obtain the precise daily station coordinates, and the coseismic displacements were estimated from the difference between averages of 4 days of GPS site positions before and after the mainshock (Hsu *et al.* 2011). The GPS measurements show coseismic horizontal displacements of up to 3.7 cm close to the hypocentre moving toward the SW and NW, whereas no eastward displacement was observed. Up to 3 cm of uplift is observed at stations to the west of the epicentre.

Five ALOS ascending SAR images collected along path 446 and two from path 447 were used to generate coseismic interferograms. All data were processed with the open source ROI_PAC 3.0 software developed and maintained at Caltech/JPL (Rosen *et al.* 2004). The 90 m Shuttle Radar Topography Mission (SRTM) DEM is used to correct the phase due to topography. Phase unwrapping relied on the branch cut algorithm in ROI_PAC 3.0. The ALOS PALSAR signal has a relatively long wavelength (L band, about 24 cm) and obtains reliable phase-change measurements even in densely vegetated areas and mountains. We processed four coseismic interferograms in two ascending-orbit paths. However, some of the interferograms are highly perturbed by ionosphere-correlated noise that can bias the result of the geodetic inversion, so only two interferograms are used. The coseismic pairs for both paths 446 and 447 (Fig. 2b) show range displacement towards the satellite west of the hypocentre, which indicates that the fault plane is located west of the hypocentre. The coseismic deformation area is about 400 km^2. On the other hand, some increasing range changes in the south and north of the coseismic deformation could be due to

Downloaded from http://gji.oxfordjournals.org/ at University of California, Berkeley on August 15, 2013

tropospheric artifacts. Near-field GPS measurements are converted into slant range displacement (SRD) and show good agreement with the InSAR results (triangles in Fig. 2b). Note that the InSAR data set contains about 4 months of postseismic deformation. Given the agreement between the GPS and InSAR results, it is reasonable to assume that the contribution of postseismic deformation to the InSAR measurement is negligible.

3 TAIWAN VELOCITY STRUCTURE, SOURCE DEPTH AND THE MOMENT TENSOR SOLUTION

The seismic velocity structure from western to eastern Taiwan observed in tomographic studies has a strong lateral heterogeneity (e.g. Wu *et al.* 2007), which is correlated with a change of the topography (Fig. 1b). Hence, a simple 1-D velocity model may not allow for fitting all the seismic station data. In order to increase the accuracy of the seismic inversion, we construct two 1-D velocity structures to represent western and eastern Taiwan, which we use for stations in either region. To obtain the two velocity models, we rely on data from the largest aftershock with known focal mechanisms and similar distance. Cohee & Beroza (1994) pointed out that aftershocks from similar distances as the mainshock can be modeled to find the velocity model and frequency range over which theoretical Green's functions are most accurate. Hence, we use the improved velocity structures, and determine the pass band frequencies for the mainshock waveforms based on the pass band frequencies applied for the aftershock inversion. The largest aftershock (M_w 5.0) occurred about 8 hours after the mainshock and is located about 8 km west of the epicentre. The reported location and depth (from CWB and Huang *et al.* 2011) are similar to the mainshock, and the CWB focal mechanism is also similar to the mainshock (strike: 323°, dip: 33°, rake: 77°). To improve the velocity structure, we use an initial 1-D velocity model proposed by Chi & Dreger (2002) as a reference model, and vary the *Vp* and *Vs* values and the number of layers to fit the aftershock seismograms given the known focal mechanism. We apply full waveform inversion using the quasi Newton method (Tarantola 2005) to find optimum 1-D velocity structures for western and eastern Taiwan. In the inversion, we compute the partial derivative Green's function wavefields with respect to *P*- and *S*-wave velocity of each layer and their Fréchet derivatives using the finite difference method. The Green's functions were computed with forward frequency wavenumber integration (e.g. Wang & Herrmann 1980; Saikia 1994). The gradient vector is scaled by the inverse of the pseudo-Hessian matrix, which is the diagonal component of the approximated Hessian matrix (Shin *et al.* 2001). For additional stability of the inversion, a small amount of damping is added to the pseudo-Hessian matrix as 1–3 per cent of the maximum value of the diagonal elements in the pseudo-Hessian matrix. We fix the bandpass filter at 0.03–0.3 Hz because this pass band maintains a relatively higher variance reduction (VR) of the aftershocks (Yoo *et al.* 2010). Given the fact that the source of the mainshock generally has lower frequency due to longer rise time and finite-source rupture durations, 0.3 Hz is an adequate choice for the upper frequency limit for the mainshock. Additionally, frequencies greater than 0.3 Hz are sensitive to structural complexity between the stations and the source that is not captured by the two simple 1-D velocity models for western and eastern Taiwan.

The fitting to the aftershock waveforms obtained at stations in western and eastern Taiwan is shown in Fig. 3. According to the best-fitting model, the Moho depth is 35 and 40 km in western and eastern Taiwan, respectively. The *P*- and *S*-wave velocities in western Taiwan are slower above 15 km depth, which is probably due to the thicker sedimentary layers. However, the west-Taiwan velocities become slightly faster in the 15–40 km depth range. This feature is also apparent in the tomographic 3-D velocity model of Wu *et al.* (2007). The values of the western and eastern Taiwan velocity models are listed in Table 1.

To determine the depth of the mainshock, we apply a moment tensor inversion method (Pasyanos *et al.* 1996; Minson & Dreger 2008) to estimate the deviatoric moment tensor solution including the strike, dip, rake and the percentage of double-couple (DC) and CLVD (compensated linear vector dipole) components. We used data from 6 BATS broad-band stations for the inversion. The residual (L2-norm) and the DC component percentage (*Pdc*) can be

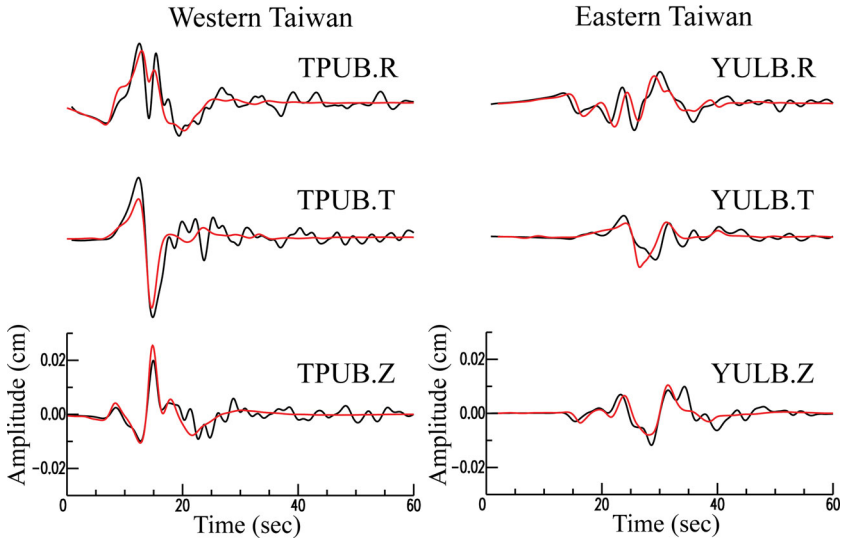

Figure 3. Waveform fitting of the largest aftershock using the velocity models for western and eastern Taiwan. TPUB and YULB (locations shown in Fig. 1b) are representative broadband stations in west and east Taiwan. R, T and Z represent the radial, transverse and vertical components. The waveforms are bandpass filtered to 0.03–0.3 Hz.

Downloaded from http://gji.oxfordjournals.org/ at University of California, Berkeley on A 13

Table 1. The one-dimensional velocity model used in this study.

Thickness (km)	*Vp* (km s^{-1})	*Vs* (km s^{-1})	Density (kg m^{-3})	*Qp*	*Qs*
		West Taiwan			
5	4.2	2.3	2400	300	100
10	4.9	2.9	2680	600	300
15	6	3.7	2680	600	300
5	6.9	4.1	2680	600	300
100	7.8	4.5	3300	600	300
		East Taiwan			
2.5	4.3	2.5	2400	300	100
12.5	5.7	3.3	2400	600	300
15	5.8	3.4	2680	600	300
10	6.4	3.6	2680	600	300
100	7.8	4.5	3300	600	300
		Chi and Dreger (2004) 1D model			
2.2	4.5	2.6	1800	200	100
2.2	4.85	2.8	2050	600	300
2.2	5.3	3.06	2250	600	300
2.2	5.6	3.23	2390	600	300
4.5	5.84	3.37	2500	600	300
4.5	6.13	3.54	2640	600	300
7.5	6.28	3.63	2700	600	300
8.5	6.6	3.81	2850	600	300
5	6.87	3.97	2970	600	300
21.5	7.43	4.29	3300	600	300
25	7.8	4.5	3300	600	300

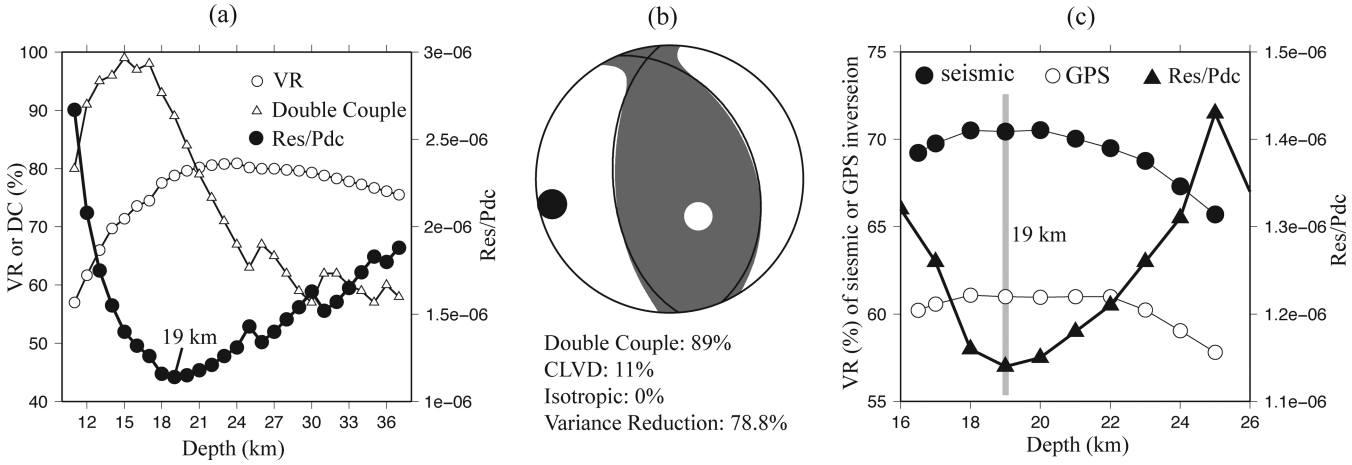

Figure 4. The determination of the moment tensor solution of the Jia-Shian event. (a) The variance reduction (VR), DC component and residual/DC (Res/Pdc) curves versus source depth. The lowest Res/Pdc value is at 19 km depth. (b) The focal mechanism at 19 km depth using the moment tensor inversion based on Pasyanos *et al.* (1996) and Minson & Dreger (2008). (c) Plot of centroid depth versus VR and Res/Pdc. Both seismic and GPS finite source inversions (circles) have higher VR when the source is in the depth range of 18–20 km. The Res/Pdc (triangles) from Fig. 4(a) is lowest when the source depth is 19 km shown by the grey line.

evaluated with depth and can provide a better estimate of the source depth by examining the ratio of the residual over the *Pdc* for different depths. The best depth in this case has the smallest residual and largest percent DC. All of the waveforms are bandpass filtered into the 0.02–0.05 Hz frequency range. The eastern Taiwan 1-D velocity structure derived using the method described in the previous paragraph is used to generate the Green's functions for the moment tensor inversion. The result shows that the highest VR (80.8 per cent) is obtained when the source depth is 23 km, which is close to the inferred source depths of Ching *et al.* (2011) and Huang *et al.* (2011). However, the moment tensor solution at this depth has only 65 per cent of DC component (Fig. 4a), which is below the expectation for a subduction/collision tectonic setting such as in western Taiwan. On the other hand, the solution with the highest DC component (99 per cent) is located at 15 km depth, with only 71 per cent VR. In order to better balance the trade-off between VR and Pdc, we estimate the ratio of the residual and Pdc. The most reliable solution lies where the residual/Pdc is a minimum. As shown in Fig. 4(a), the lowest residual/Pdc value is at 19 km in depth, about 3 km shallower than found in previous studies of this event (e.g. Ching *et al.* 2011; Huang *et al.* 2011). The focal mechanism (Fig. 4b) based on this source depth shows 89 per cent DC component with the NE-dipping nodal plane having strike, dip and rake values of 322°, 28° and 60°, respectively. This strike and dip of the DC component of the moment tensor solution and the centroid depth of the source are then used for the finite source inversions. The seismic moment obtained from the moment tensor inversion is 1.69 $\times 10^{18}$ N m corresponding to M_w 6.1.

Downloaded from http://gji.oxfordjournals.org/ at University of California, Berkeley on August 15, 2013

4 INVERSION METHOD AND RESULT

We rely on a linear least squares inversion code based on the method of Hartzell & Heaton (1983) in which the finite source is discretized with a finite distribution of point sources in both space and time. We use a damped, linear least squares inversion with a slip positivity constraint to determine the spatiotemporally distributed slip. The waveforms are bandpass filtered to 0.03 to 0.3 Hz, which is determined from the aftershock fitting described in Section 3. Based on an empirical relationship between the rise time (T_R) and the seismic moment (Somerville *et al.* 1999; modified for SI units Dreger & Kaverina 2000), $T_R = 4.37 \times 10^{-7} \times {M_0}^{1/3}$ (SI units). Thus, given our seismic moment from the moment tensor inversion, $M_0 = 1.69 \times 10^{18}$ N m, the rise time is $T_R = 0.5086$ s. As a result, we use a single time window with a fixed rise time of 0.5 s. Although we use the rise time from the empirical relationship, the frequency band determined from the velocity structure modeling of the aftershock data precludes the resolution of rise time for values less than 3 seconds. This implies that we cannot resolve the rise time we apply it to account for the phase delay. The choice of rupture velocity will be tested and discussed in Section 4.4. Spatial smoothing with linear equations minimizing differences in slip between subfaults is applied to stabilize the seismic and geodetic inversion. Different weighting and smoothing parameters are applied to the simultaneous inversion using the method proposed by Kaverina *et al.* (2002). The Green's functions for western and eastern Taiwan are obtained from fitting the largest aftershock as described in Section 3. The seismic Green's functions were computed every 2 km from a distance of 20–100 km and every 1 km from a depth of 13–25 km using a frequency wavenumber integration code by Saikia (1994) based on the method of Wang & Herrmann (1980).

Absolute time shifts between the Green's functions and the observed data may be caused by the use of the simplified velocity model (Kim & Dreger 2008). To reduce this problem, we first perform forward modeling based on a point source focal mechanism with a moment equivalent to a M_w 6.3. The starting time of this point source is based on the CWB solution, so we can then line up the first shear wave arrival between the predicted and observed waveforms by shifting the predicted waveforms. We note that the applied time-shift correction of the three components should be the same at a single seismic station, but can differ between stations. The reason of the time shift is mainly due to lateral velocity variations and depends on the distance from the source to the seismic station. We determine the time shift corrections for both TSMIP and BATS stations, as listed in Table 2.

For the geodetic inversion, the geodetic Green's functions are computed using the programs EDGRN/EDCMP (Wang *et al.* 2003). This allows for the calculation of the Green's functions relating unit slip on each source subfault dislocation to surface displacements in a layered elastic model over a half-space. However, this calculation does not consider lateral variations of elastic structure. Thus we use the east Taiwan model derived from fitting the waveforms described earlier to compute the Green's functions for Taiwan (Table 2), since the hypocentre and most of the coseismic slip are located in the Central Range that belongs to the east Taiwan velocity model.

We construct a 50 × 50 km NE dipping fault plane with 625 (25 × 25) subfaults for the finite source inversions. The initial location of the fault centre is set to be the hypocentre, and the fault geometry is the same as the 322° striking, 28° dipping nodal plane of the DC component of the preferred moment tensor inversion result described in Section 3. We first run multiple GPS finite source inversions to obtain a more accurate fault location. We vary the horizontal location of the fault plane by a few kilometers in EW and NS components until the highest VR is reached in the GPS inversion. The depth of the fault plane is also re-estimated to reach the highest VR in either GPS or seismic inversion. The result (Fig. 4c) shows that both seismic and GPS inversions have higher VR in the depth range of 18–20 km. This range contains the depth resolved from lowest Residual/Pdc ratio of the moment tensor inversion (triangles in Fig. 4c).

The finite source inversions are first obtained using the seismic, GPS and InSAR data sets individually to compare results and determine common features. Due to the different characteristics of data and the number of data points, each inversion requires different smoothing parameters to reach the highest VR. As a higher spatial smoothing factor is applied to the inversion, a smoother result will be obtained, but the fitting to the data (VR) will be lower as well. We can depict the smoothing by plotting the smoothing factor versus VR curve, and then choose the smoothing factor beyond which the model if does not significantly decrease. We first determine the preferred degree of smoothing and obtain the peak coseismic slip for the seismic inversion. We then choose the smoothing factor for the GPS and InSAR inversions to produce a model with a comparable peak slip as the seismic inversion. In the seismic-only inversion, the chosen smoothing factor is 4×10^{-7} resulting in VR = 72 per cent (Fig. 5a). The smoothing curves versus VR for GPS and InSAR are shown in Figs 5(b) and (c). We can see that the smoothing values are 10^{-7} and 2×10^{-6} for GPS (VR: 68 per cent) and InSAR (VR: 75 per cent), respectively. By this method of choosing the degree of smoothing, we find that all three inversions obtain similar total slip area (Fig. 6). The detail of the inversion results and the joint inversion will be discussed later.

4.1 Seismic inversion

The seismic data are from broad-band stations of the BATS network and from strong motion stations (TSMIP). Only stations located on

Table 2. Station locations and time shifts.

Station	*Latitude (deg)*	*Longitude (deg)*	*Time Shift (s)*	*West or East Taiwan*	*Strong Motion or Broadband*
TTN026	22.8597	121.0916	0.0	East	Strong Motion
TTN052	22.5956	120.9620	−0.5	East	Strong Motion
TTN051	23.1864	121.0253	1.0	East	Strong Motion
CHY102	23.2442	120.6226	0.0	West	Strong Motion
KAU049	22.7442	120.6399	0.5	East	Strong Motion
CHY074	23.5087	120.8131	0.0	West	Strong Motion
TTN053	22.3814	120.8569	0.6	East	Strong Motion
MASB	22.6109	120.6326	−0.5	East	Broadband
YULB	22.3900	121.2970	−0.8	East	Broadband
SSLB	23.7870	120.9540	0.0	West	Broadband

Downloaded from http://gji.oxfordjournals.org/ at University of California, Berkeley on A 13

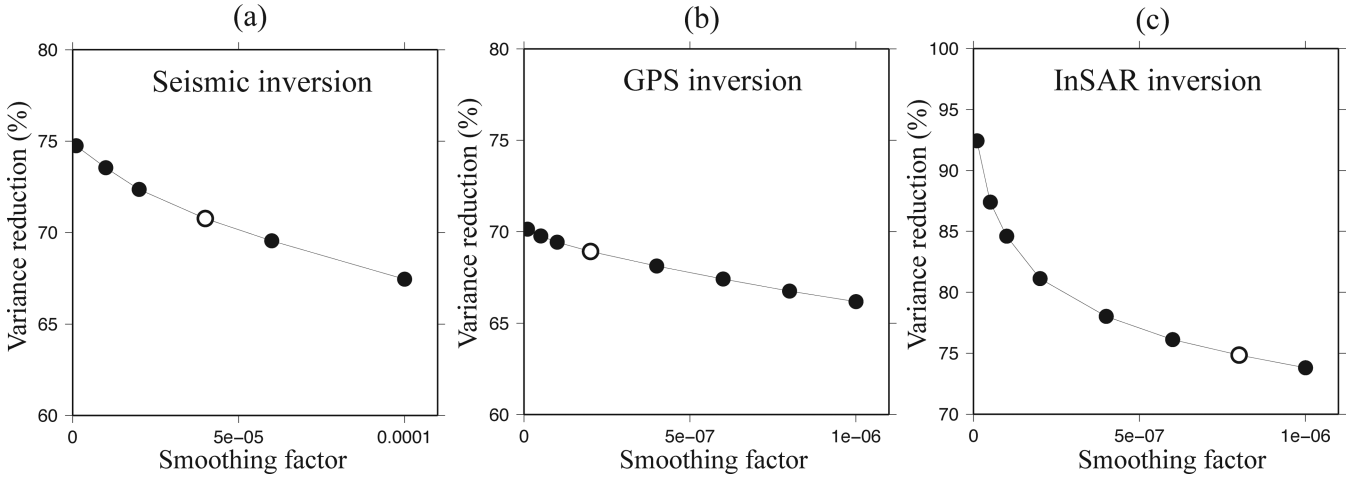

Figure 5. Variance reduction as a function of smoothing factors applied to individual (a) seismic, (b) GPS and (c) InSAR inversions.

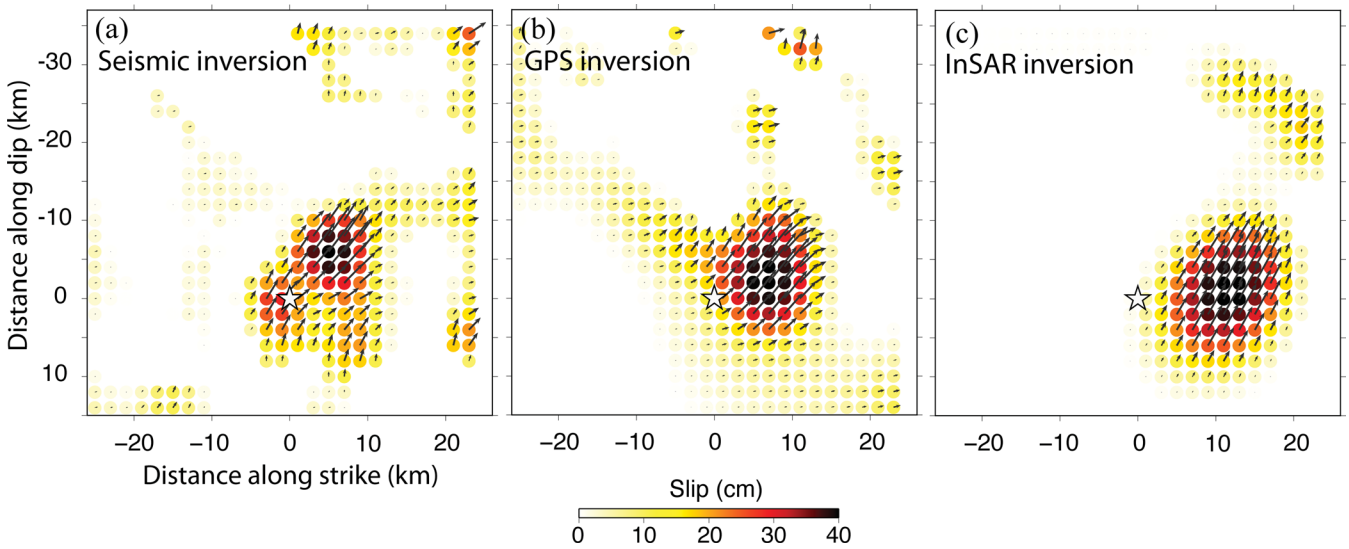

Figure 6. Coseismic slip model obtained from (a) 10 seismic stations (peak slip: 33.5 cm; total moment: 3.46×10^{18} N m; VR: 76 per cent), (b) GPS (peak slip: 34.7 cm; total moment: 3.29×10^{18} N m; VR: 69 per cent), (c) InSAR (peak slip: 30.4 cm; total moment: 3.35×10^{18} N m; VR: 71 per cent). The black arrows represent the slip direction and amplitude of each subfault. Note that the inversions from different data sets have different spatial distribution, but they all have a 15 km × 15 km coseismic slip zone northwest of the epicentre (grey star).

bedrock are selected for the inversion to prevent model artifacts due to site effects for stations located on sedimentary basins. We choose 7 strong motion stations providing near field observations and 3 BATS stations for the far field. The E–W, N–S and vertical waveforms are all used in the seismic inversion; thus we have 30 components of seismic data. We apply the same bandpass filter (0.03–0.3 Hz) to both data sets prior to the seismic inversion. As described before, we correct the time shift based on point source forward modeling, and use two different 1-D velocity models for the stations located in west and east Taiwan. The depth of the hypocentre is determined by the moment tensor solution (see Section 3 and Fig. 4). The rise time is fixed to 0.5 second (see Section 4), and determination of the rupture velocity is described in Section 4.4.

The model obtained in the seismic inversion fits both the strong motion data and the broadband data very well (Fig. 7). The result of the seismic inversion shows the main slip asperity is located near and mostly above the earthquake hypocentre. The primary coseismic slip area is about 15 km × 20 km (the light yellow to dark red area near the star in Fig. 6a), and there are two peak slip regions in this area, with about 34 cm and 24 cm of slip, respectively. In addition to the main asperity at the source depth (~20 km), there is an additional asperity near the upper part of the fault plane that has coseismic slip of less than 10 cm at about 4 km depth. There are some other minor slip areas located on the edge of the fault plane that might be due to the uneven distribution of seismic stations. The stability of the minor slip asperities in the model is tested in the station sensitivity and resolution tests in Section 5, and is found to be more stable near the hypocentre and the near surface. The rake is variable on the each sub fault and ranged from 15° to 105°, but most of the sub faults, and those with significant slip, have a rake angle of about 60°. The total moment obtained from the seismic inversion is 3.46×10^{18} N m, which is equivalent to a M_w 6.3 earthquake. The VR of the best fitting inversion is 72 per cent with a smoothing factor of 4×10^{-5} (Fig. 5a).

Downloaded from http://gji.oxfordjournals.org/ at University of California, Berkeley on August 15, 2013

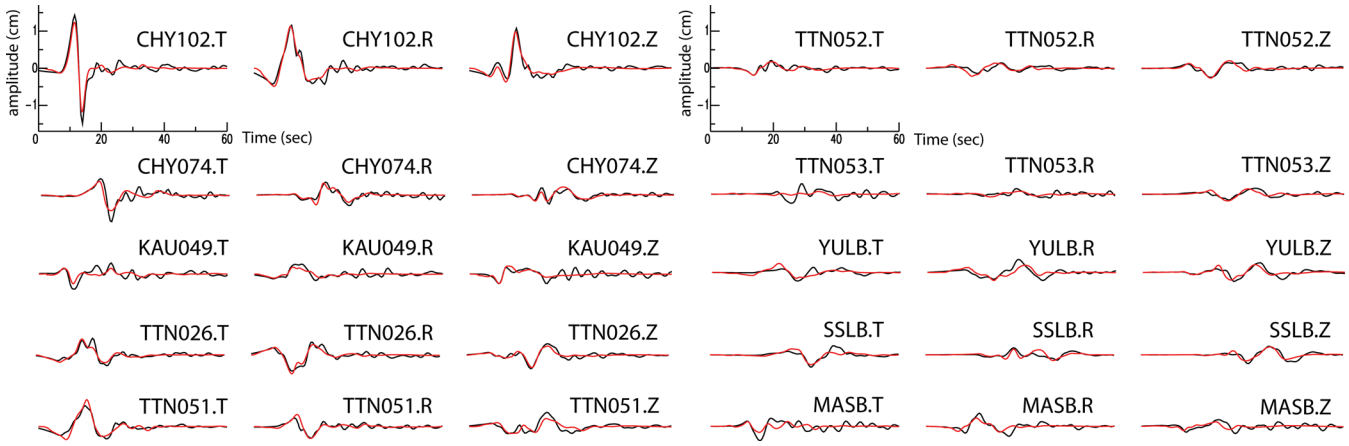

Figure 7. Comparison of synthetic waveforms (red) and the data (black) using only seismic inversion. CHY102, CHY074, KAU049, TTN026, TTN051, TTN052 and TTN053 are strong motion stations. YULB, SSLB and MASB are broadband stations. All of the waveforms are bandpass filtered to 0.03–0.3 Hz. For the locations of all stations see Fig. 1(b). Note that station TPUB is not used here because the data are clipped in the main shock.

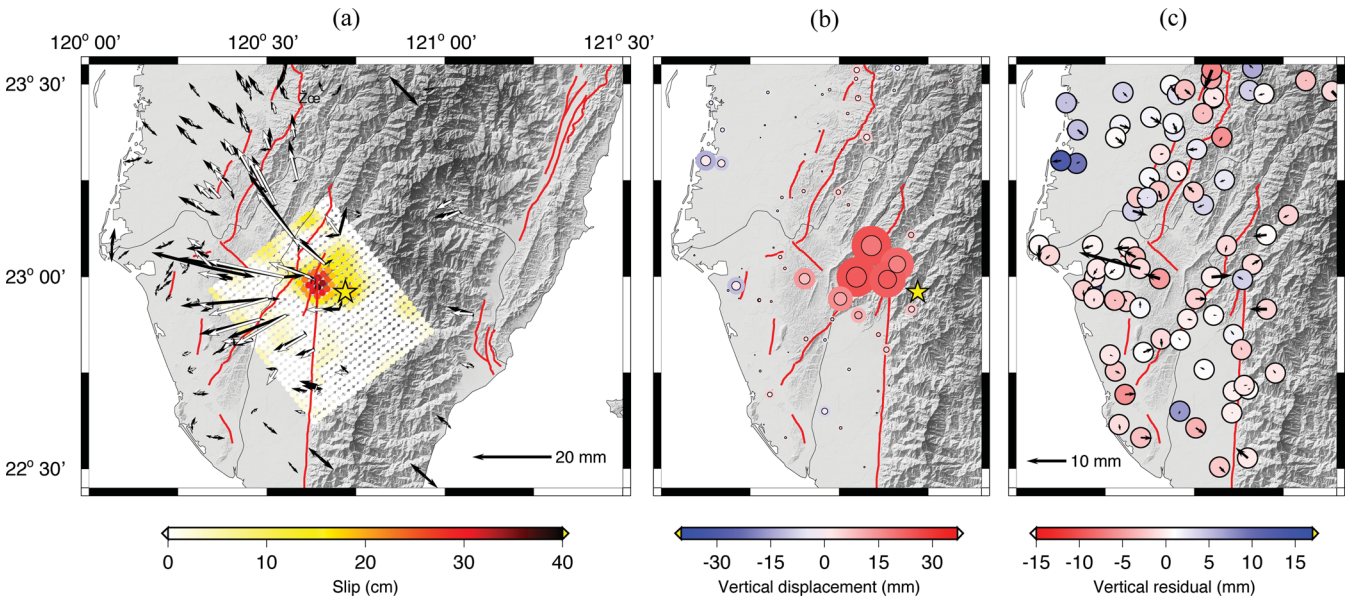

Figure 8. GPS-only inversion. (a) The black and white arrows represent the horizontal data and predictions, respectively. The colour-contoured grid represents the coseismic slip model projected to the surface. (b) The colour of the circles represent the vertical coseismic displacement. The circles without outlines and the circles with black outlines are the data and predictions, respectively. (c) The arrows and circle colours show the residuals between the GPS data and model predictions.

4.2 Geodetic inversion

4.2.1 Individual GPS and InSAR inversions

In the geodetic inversions we do not need to specify the hypocentre, rise time and rupture velocity, since both GPS and InSAR data reflect the final static surface displacement and are independent of the source time history. The result of the GPS inversion based on 3-D displacements at the 108 continuous GPS stations is shown in Fig. 6(b). The total moment is 3.29×10^{18} N m, which is also equivalent to a M_w 6.34 event. As described earlier, the smoothing factor for the geodetic inversion is chosen to obtain the same peak slip as the seismic-only inversion. The smoothing factor versus VR plot is shown in Fig. 5(b). The main slip asperity is located northwest of the epicentre, and the slip area is about 13 km × 15 km. The seismic and GPS inversions result in very similar models in terms of the primary slip asperity and the total moment. However, the GPS inversion also shows an additional slip asperity on the shallower part of the fault plane that is similar to the seismic inversion. This provides supporting evidence for this minor asperity, because it is indicated by two completely independent data sets.

Fig. 8 shows the result of the predicted coseismic displacements based on the GPS only inversion model. The GPS residuals are 2.7, 1.8 and 4.5 mm in the east, north and vertical components, respectively (Fig. 8c). The misfit in the far-field is generally smaller than 5 mm which is within the uncertainty of the GPS data. In the vertical, larger residuals are observed in the coastal area that might be due to land subsidence that is independent of the earthquake, even though the misfit is still within the vertical uncertainties (6.8 mm, estimated from Hsu *et al.* 2011). Since the coseismic GPS observation is the difference of the 4-day average positions before and after the mainshock, the coseismic observation may be contaminated with early postseismic transients (Hsu *et al.* 2011). However, since the coseismic slip distribution from the GPS inversion is very similar to that revealed by the seismic inversion, the postseismic

Downloaded from http://gji.oxfordjournals.org/ at University of California, Berkeley on A 13

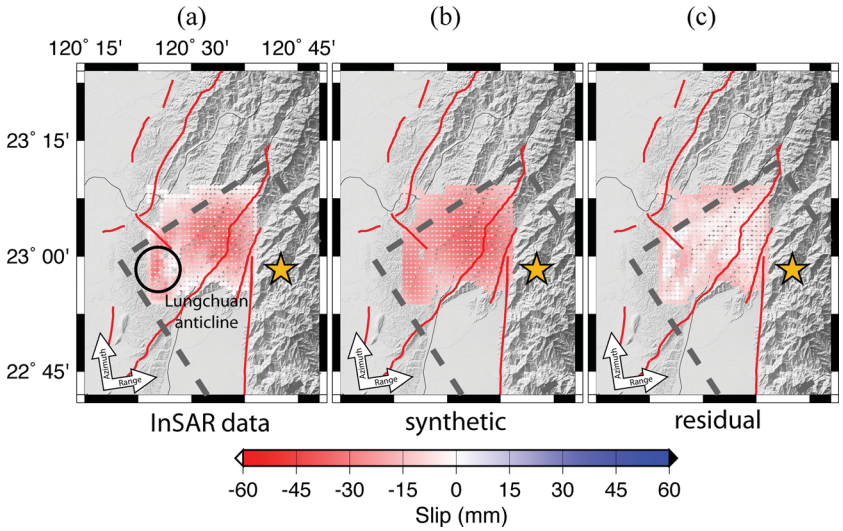

Figure 9. Observed, predicted and residual InSAR displacements from InSAR-only inversion. (a) Coseismic InSAR measurements after downsampling and noise reduction (see text). The spatial resolution is about one pixel per km^2. (b) InSAR model prediction with the same colour scale. (c) Difference between the observed and predicted InSAR observations. The orange star represents the epicentre of the earthquake, and the grey dashed lines represent the outline of the fault model.

Table 3. ALOS SAR images.

	Track	
	446	447
Acquisition dates	100108–100711	100125–100728
Bperp (m)	564	614.5
Time span (days)	185	185

surface displacements during the first 4 days must have been very small.

For the InSAR inversion (Fig. 9), the InSAR coseismic measurement is taken from the average of two coseismic interferograms (one from track 447 and one from track 446, see Fig. 2b, Table 3). In order to reduce the effects of atmospheric or topography related noise, and to focus on the coseismic change, we only consider the area where the InSAR coseismic surface displacements are significant. We also down-sample the interferogram into about one pixel per square kilometer to reduce the calculation time. We consider the InSAR signal in an area of about 25 km × 25 km with 601 InSAR data points in total (Fig. 9a). The InSAR-only inversion result (Fig. 7c) also shows one main asperity NW of the hypocentre with a circular area of about 6 km radius. The peak slip is 30.3 cm and the rake of the slip is generally 60°, consistent with the seismic and GPS inversions. The InSAR-derived coseismic slip is smoother than the other inversions because of a smaller spatial data coverage and a median filter with 1.2 × 1.2 km window size applied to the InSAR data. However, due to the denser data spacing of InSAR in the given area, the detail of the surface displacement is well preserved (some localized surface change in Fig. 9a). Hence, even though the slip distribution is smoother than in the other inversions, the slip asperities are more reliable. The InSAR inversion also shows a minor slip asperity in the shallower part, but the location of this small slip area is about 2 km deeper than in the other inversions. The zone of InSAR surface displacement corresponding to this minor asperity occurred along the Lungchuang anticline (Fig. 9a). If this minor asperity is the same as the one inferred from seismic inversion, we can conclude that this shallow slip is coseismic and the Jia-Shian earthquake ruptured to shallow depths of about 5 km in the southwest below this geologic structure.

4.2.2 GPS and InSAR combined inversion

For the geodetic inversion, we need to invert both GPS and InSAR data with proper weighting and smoothing parameters for both. We first fix the GPS weighting as one and change the InSAR weighting from 0 to 2 to find a higher VR for both data sets. The result (Fig. 10a) shows a decrease of GPS VR while increasing InSAR weighting. However, the increase of InSAR VR is less significant when InSAR weighting is higher than 0.2. The InSAR weighting is chosen as 0.1 because there is a substantial increase of the VR for InSAR as the weight increases from 0 to 0.1 but only a little decrease of GPS VR. We test InSAR weighting as 0.1 or 0.2, and vary the smoothing of the geodetic inversion from 10^{-8} to 10^{-6} (Fig. 10b), but we keep the InSAR weighting as 0.1 because it does not significantly decrease the GPS VR as when 0.2 does. The smoothing factor is determined by finding the smoothest model that does not decrease VR significantly (Kaverina *et al.* 2002). From this criteria we determine the smoothing factor as 2×10^{-7}, so the geodetic joint inversion (Fig. 11a) has a similar pattern as the individual inversions (Fig. 6). The total moment estimated from the geodetic inversion is 3.3×10^{18} N m and the peak slip is 39.8 cm. The pattern of the slip model is similar to the GPS inversion.

One main difference between GPS and InSAR inversion results is that the main slip area in the InSAR inversion is shifted by 2 km to the west, even though both obtain a similar area for the main slip asperity. However, according to the trade-off curve in Fig. 10(b), shifting the main slip asperity, that is, changing the InSAR weighting from 0 to 0.1 or 0.1 to 0.2 only increases the VR of InSAR by 6 or 3 per cent, so the InSAR inversion is not very sensitive to the location of main asperity within the range of the 1–2 km shift. Thus, the geodetic inversion finds the main asperity close to that of the GPS-only inversion.

4.3 Joint inversion

For the joint inversion, we keep the same weighting ratio between GPS and InSAR (GPS weight = 10 × InSAR weight) as in the geodetic inversion, we then change the weighting of geodetic data from 0.5 to 5 with a constant weighting the seismic data

Downloaded from http://gji.oxfordjournals.org/ at University of California, Berkeley on August 15, 2013

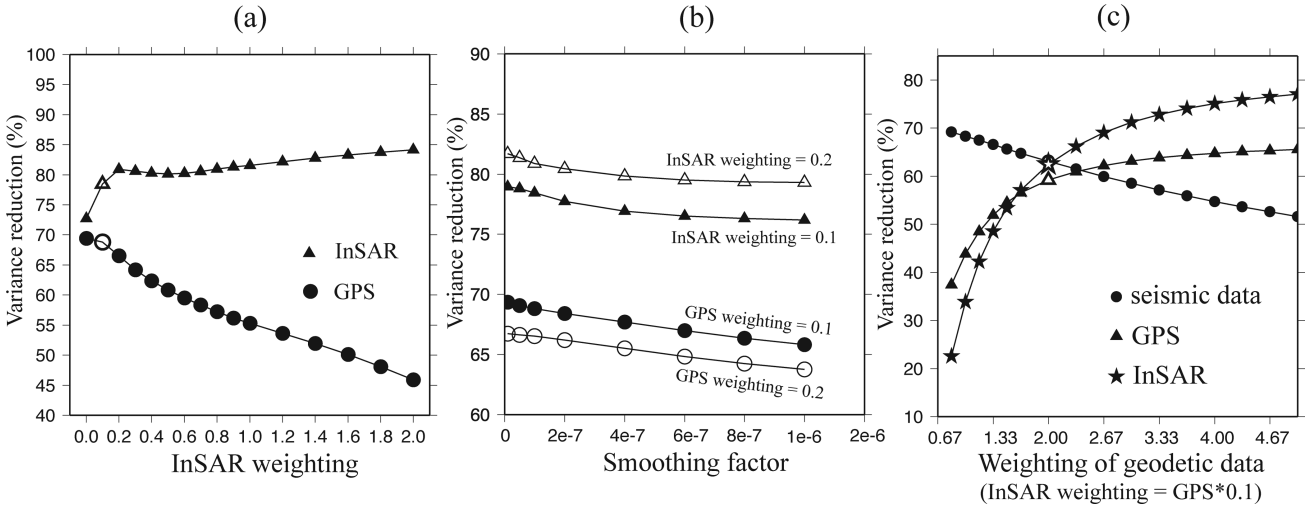

Figure 10. Tests of weighting and smoothing for geodetic and joint inversions. (a) Different InSAR weighting with GPS weighting fixed to one versus *VR*. The white triangles and circles represent the range of preferred weights of the InSAR data. (b) Tests for the smoothing factor to the geodetic inversion. Triangles and circles show VR of InSAR and GPS data, respectively. White and Black symbols represent InSAR weighting of 0.2 and 0.1, respectively. (c) Weighting of each data set versus VR. The weighting of seismic data is fixed to 1, and the InSAR weight is 10 per cent of the GPS weighting.

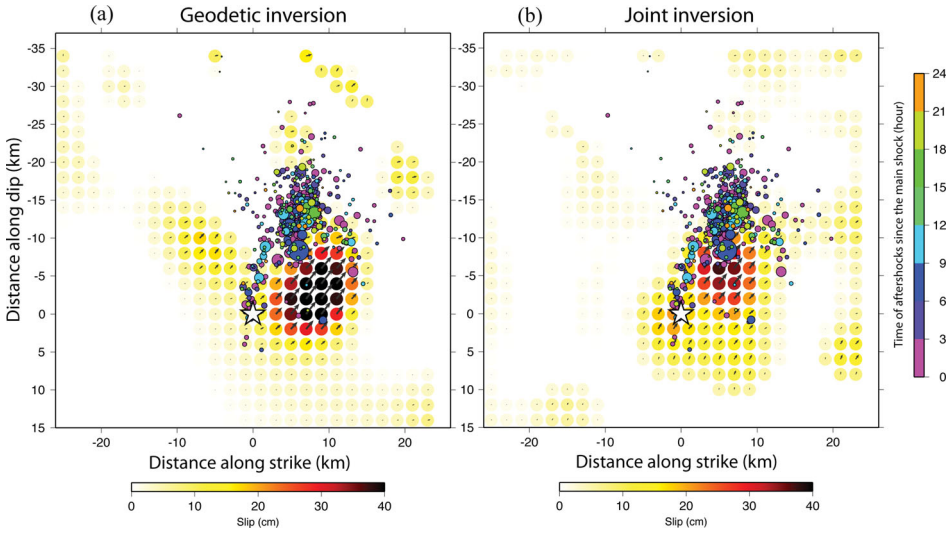

Figure 11. Coseismic slip model obtained from (a) geodetic inversion (peak slip: 39.8 cm; total moment: 3.30×10^{18} N m; GPS VR: 68.8 per cent, InSAR VR: 78.4 per cent), (b) Joint inversion (peak slip: 42.5 cm; total moment: 3.25×10^{18} N m; seismic VR: 74.8 per cent, GPS VR: 64.9 per cent, InSAR VR: 77.0 per cent). The black arrows represent the slip direction and amplitude of each subfault. The coloured circles are the aftershocks since the main shock in hours.

(weight = 1). As shown in Fig. 10(c), the VR for the geodetic data increases rapidly as the weight of the geodetic data increases from 0.5 to 5.0, whereas the VR of the seismic data decreases from 70 per cent to about 50 per cent. We choose a weight of the geodetic data of 2.0 from visual inspection of the tradeoff in fitting the respective data sets. Consequently, the VR for the seismic, GPS and InSAR data in the joint inversion are 74.8, 64.9 and 77.0 per cent, respectively (Fig. 10c).

The result of the joint inversion is shown in Fig. 11(b). Not surprisingly, we find a similar main slip asperity as in the individual and geodetic inversions (Figs 6a to c and 11a). The peak slip and the area of the main asperity are 42.5 cm and about 200 km^2, respectively. The total moment of the joint inversion is 3.25×10^{18} N m, which is equivalent to a M_w 6.34 event. Given the mean slip of 15 cm on a 20 km × 25 km main asperity (Fig. 11b), the static stress drop of the Jia-Shian event is 0.24 MPa. This value of stress drop is at least ten times smaller than the 1999 Chi-Chi earthquake (6.5 or 22.5 MPa, Huang *et al.* 2001; Ma *et al.* 2001) and its aftershocks (Chi & Dreger 2004), and in the low range of global average stress drops for reverse events (Mai & Beroza 2000; Allmann & Shearer 2009). Some minor asperities are seen in the shallower part, but also in the western and bottom edges. The first 24 hours aftershocks are plotted onto the geodetic and the joint inversions. Most of them lie along the upper periphery of the main asperity, which implies that the aftershocks occurred along the margin of the coseismic rupture. Most of the aftershocks shown in Fig. 11 occurred in the first 12 hours.

4.4 Rupture velocity from seismic data

The rupture velocity is examined for seismic-only and the joint inversions in order to evaluate the stability of the inversion associated with the combined data. As shown in Fig. 12, the rupture velocities

Downloaded from http://gji.oxfordjournals.org/ at University of California, Berkeley on A 13

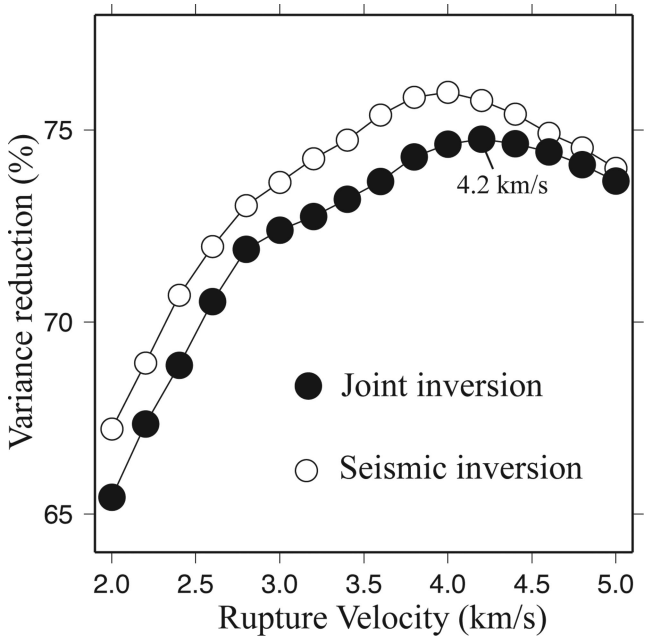

Figure 12. The variance reduction versus rupture velocity. The white circles are the seismic only inversion and the black circles are the VR of seismic data in the joint inversion. The rupture velocity used in this study is 4.2 km s^{-1}.

producing higher VR are in the range of 3.8–4.4 km s^{-1} for seismic VR for both seismic only and joint inversions. The preferred rupture velocity is somewhat higher in the joint inversion than in the seismic inversion, but the fitting curves are quite similar (Fig. 12). This shows that considering the geodetic data, which do not contain time dependent information of the earthquake source, does not change the inferred rupture velocity much. The preferred rupture velocity range is higher than the shear wave velocity in either west or east Taiwan (3.7 and 3.4 km s^{-1}, respectively). A rupture velocity between the shear wave and *P*-wave velocity can be interpreted as a supershear event (Walker & Shearer 2009). In comparison, the rupture velocity obtained for other recent earthquakes in Taiwan such as the 1999 M_w 7.6 Chi-Chi earthquake in Central Taiwan and its larger aftershocks is much lower. The rupture velocity of the Chi-Chi mainshock is about 2.0 km s^{-1} (Ji *et al.* 2003) and 1.5–3.2 km s^{-1} for the larger aftershocks (M_w 5.8 to 6.3) that occurred in the month following the mainshock (Chi & Dreger 2004). Most of the Chi-Chi aftershocks are shallow events with source depth less than 16 km, except one at 18 km (Chi & Dreger 2004). The Jia-Shian event is located deeper than the earthquakes in Central Taiwan, so the larger rupture velocity and deeper location of this event may reflect a different geological setting.

Supershear ruptures are quite rare. At least two supershear cases are found in the 2001 M_w 7.8 Kokoxili (Bouchon & Vallée 2003) and the 2002 M_w 7.9 Denali events (Dunham & Archuleta 2004; Ellsworth *et al.* 2004; Dunham 2007). Walker & Shearer (2009) found a rupture velocity close to the P wave velocity (∼5.6 km s^{-1}) for these two events. The supershear rupture velocity for these events is between $\sqrt{2} \times Vs$ and Vp, whereas the rupture velocity for the Jia-Shian event is only $1.23 \times Vs$. One interpretation is that supershear rupture velocity requires propagation for a certain distance up to which the rupture velocity is still about $0.8 \times Vs$, and it will jump to $\sqrt{2} \times Vs$ or higher velocities after this initial distance (Walker & Shearer 2009). In other words, the rupture velocity history is not a constant and can be quite complex. In our inversion we assume a constant rupture velocity resulting in a value between the Rayleigh wave velocity (2.72 km s^{-1}) and $2 \times Vs$ (4.8 km s^{-1}), which may decrease the maximum rupture velocity. We also test the inversion with Rayleigh wave velocity as the rupture velocity and find a rougher slip distribution and smaller slip area given the same smoothing (Fig. S4). The total VR in this model is reduced by 2.2 per cent from the best fitting model.

5 RESOLUTION AND SENSITIVITY TESTS USING SYNTHETIC DATA

We test the sensitivity and the model resolution in order to evaluate the validity of our joint inversion result and the influence on the inversion from incomplete data or inversion parameterization (e.g. incorrect rupture velocity). For the station sensitivity analysis we perform the inversion with incomplete data sets in order to investigate the solution with different distributions of stations. For the resolution test we generate an artificial rupture model similar to the Jia-Shian event to obtain synthetic waveforms and geodetic data. Different smoothing and noise, and incorrect rupture velocity are added to the synthetic data to test the resolution of the inversion results.

5.1 Stations and solution sensitivities

In south Taiwan, the seismic and GPS stations are deployed in mountain, foothill and plain areas (Figs 1b and 2a), and the InSAR data points are restricted to the relatively flat area (Fig. 2b). As a result, the topography and the geologic structure underneath the stations may add propagation complexity and affect the finite-source inversion result. Timing errors, site and 3-D propagation effects in the seismic data contribute additional sources of uncertainty to the model (Kim & Dreger 2008). In order to test the effect of the spatial distribution of data and the uncertainties of the seismic data, we randomly remove 20 per cent of the seismic, GPS, and InSAR data and repeat this process 20 times to see how much the resampled seismic and geodetic data can vary the inferred coseismic slip distribution. The average slip, standard deviation and the coefficient of variation of the slip on the fault plane from the 20 inversions are shown in Fig. 13. The slip distribution obtained from all data and the 80 per cent data subsets are very similar. The obtained standard deviation of slip of the subfaults (Fig. 13b) is generally 10 times smaller than the slip on each subfault but is larger along the bottom and west edges of the fault plane. The coefficient of variation is the standard deviation divided by the average slip, which indicates a more stable solution when the coefficient is lower. The coefficient of variation of each subfault (Fig. 13c) shows that the coefficient is less than 30 per cent in the main asperities (the asperity near the hypocentre and the upper right of the fault plane), which indicates that these asperities represent stable features of the slip models.

The average total moment obtained from the 20 subsampled data sets is 3.22×10^{18} N m with a standard deviation of 1.18×10^{17} N m, and the coefficient of variation is equal to 3.67 per cent. The total moment based on the 80 per cent data subsets is very close to that based on the joint inversion (3.29×10^{18} N m). The VR of the 80 per cent data are 71.7 per cent (standard deviation, *std*: 2.23 per cent), 66.4 per cent (*std*: 4.72 per cent) and 76.2 per cent (*std*: 1.27 per cent) for the seismic, GPS and InSAR data, respectively. These values are very close to the joint inversion with all of the data (74.8, 64.9 and 77.0 per cent for seismic, GPS and InSAR, respectively, Fig. 10c). However, it is notable that the coefficient of

Downloaded from http://gji.oxfordjournals.org/ at University of California, Berkeley on August 15, 2013

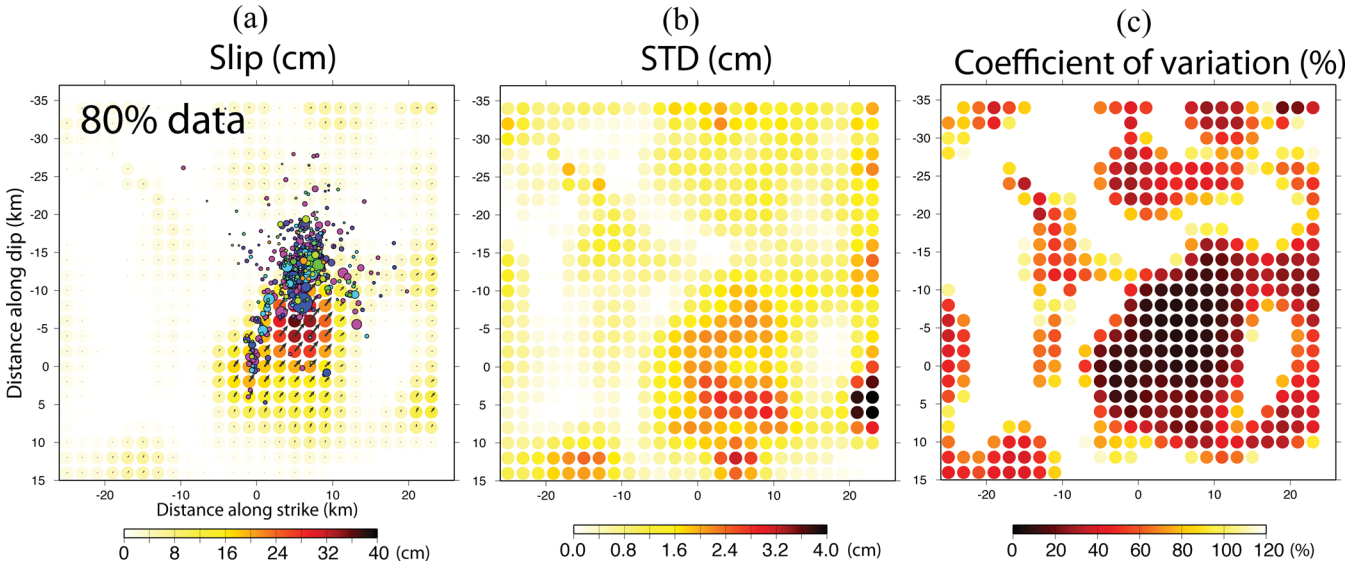

Figure 13. Sensitivity test of inversions using 20 repeated samples of 80 per cent of seismic, GPS and InSAR data. (a) average slip, (b) standard deviation and (c) coefficient of variation. The mean total moment is 5 per cent larger than the total moment obtained in the inversion of all of the data (Fig. 11b) 4.

variation of slip for the GPS data (7.11 per cent) is much higher than that for the seismic (3.11 per cent) or the InSAR data (1.68 per cent), so it appears that the GPS data have less sensitivity to slip than the other two data sets. Indeed, given the uncertainties of the GPS about 0.25 cm in horizontal and 0.7 cm in vertical based on the GPS data of Hsu *et al.* (2011), the coseismic displacement in the far-field stations may be lower than their noise level. So the random removal of 20 per cent GPS data (including both far- and near-field stations) can increase the GPS model variance more than in either of the seismic or InSAR tests. For InSAR data, since we down-sample the interferogram and take the average line of sight displacement from two interferograms, the data are relatively smoother than GPS or seismic data. For the seismic data, it seems that the solution is well constrained with the different station subsets, and thus station coverage does not appear to introduce a bias in the solution.

5.2 Resolution test

The resolution test investigates the sensitivity of the source model to the spatial distribution of the seismic and geodetic data. In addition, we also test how data smoothing, weighting and the noise level affect the model resolution. In this test, we use a forward slip model on the same 50 km × 50 km fault plane with 625 subfaults and a synthetic slip distribution (Fig. 14e). The rupture velocity is set to be 4.2 km s^{-1}. We use the forward model to obtain the synthetic seismic waveforms and geodetic measurements. In order to keep the same condition as in our data inversion, we keep the same weight between seismic and geodetic data as in our previous joint inversion, and then add the smoothing to the inversion and/or add random noise of 20 per cent of peak amplitude to the seismic waveforms as well as the geodetic data.

Fig. 14(a) shows the result without smoothing and noise. The variance reduction is more than 99 per cent for the three data sets, and the number of the slip asperities and the area are the same as the input model, even though the amplitude of the slip in the asperities is not fully recovered. Another test with seismic only inversion shows 100 per cent variance reduction and identical slip distribution as the input model (Fig. S5). In fact, one seismic station has 65 (sec) ×10 (sample/sec) ×3 (components) = 1950 samples, so we have 1950 × 10 (stations) = 19,500 data points for the inversion, with only 625 unknown subfaults × 2 degree-of-freedom for rake = 1250. Besides, we do not change the rise time, rupture velocity and the Green's functions, so an identical result could be obtained in the absence of noise. However, the total number of GPS or InSAR data points is less than the unknowns, so the joint inversion that requires weighting of seismic, GPS and InSAR cannot reproduce an identical inversion result. In the first test there is no smoothing applied to the inversion, so the slip on the subfaults will be assigned in order to obtain highest *VR* without considering any correlation on the adjacent subfaults (Fig. 14a). In addition, the seismic data represent finite wavelengths in the data (Kim & Dreger 2008), so the constraining equations (smoothing between the adjacent subfaults) are needed to prevent the model from over fitting the given data. As a result, some amount of smoothing needs to be applied to the inversion, even though it will decrease the fit to data. The inversion with the same smoothing as we apply in the joint inversion is shown in Fig. 14(c). The variance reduction is still very high (>99 per cent for three data sets), but now the inversion result shows the correct number of asperities and the amplitude of the slip is much closer to the input model compared to the inversion without smoothing.

Furthermore, we apply random noise scaled at 20 per cent of the peak amplitude of each synthetic waveforms and synthetic geodetic displacements (GPS and InSAR) obtained from the input model, in order to simulate the condition that the waveforms are affected by the regional heterogeneity or other site-effects. Without applying any smoothing (no constraining equations between subfaults), the result (Fig. 14b) shows a very scattered slip distribution, even though the slip areas are similar to the input model and the variance reduction is still high (98.57, 99.98 and 99.87 per cent for seismic, GPS and InSAR data, respectively). With 20 per cent noise and smoothing applied (Fig. 14d), the slip asperities are smeared out, but the peak slip is similar to the input model. This suggests that even with certain amounts of uncertainty in the seismic and geodetic data, the inversion result does not deviate from the input model. The result of this test differs from a previous study on the 2004 Parkfield, California, strike-slip rupture using the same method

Downloaded from http://gji.oxfordjournals.org/ at University of California, Berkeley on A 13

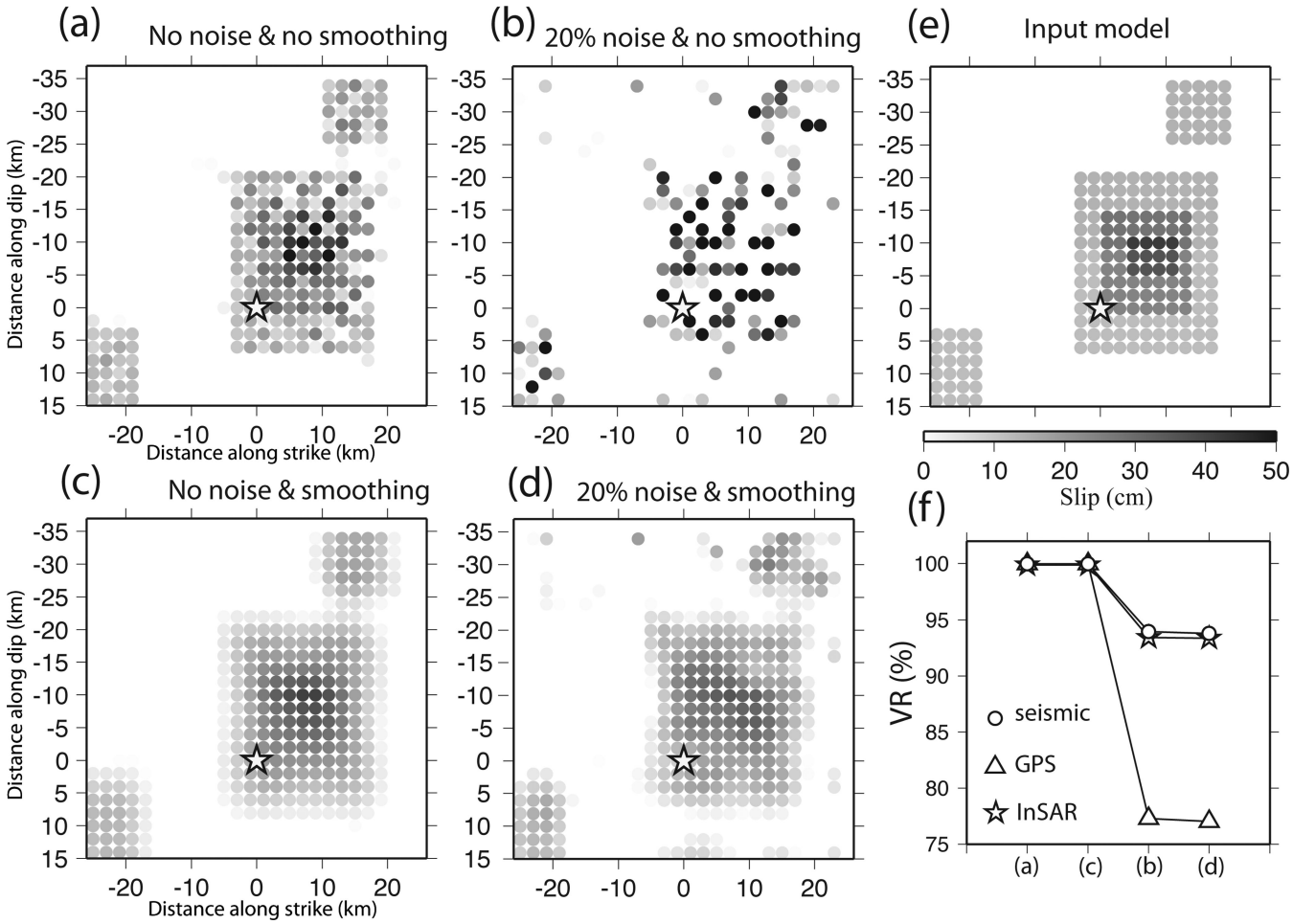

Figure 14. Synthetic resolution tests. (a) Inversion result without smoothing (constraining equations). (b) Inversion result with the smoothing. (c) Inversion result with random noise (20 per cent of the peak amplitude of seismic data, GPS and InSAR) without smoothing. (d) Inversion result with noise and smoothing. (e) Input slip model. The velocity models, rake, rise time and rupture velocity are the same as used in the joint inversion of the Jia-Shian event. (f) Variance reduction of each data set and different resolution tests.

(Kim & Dreger 2008). They found that they cannot recover the slip distribution deeper than 13 km, but our resolution test shows that the inversion can resolve the slip even at the depth of 25 km, which is likely due to our use of more distant seismic and GPS stations that provide coverage in both the near- and far-field, and because we include the vertical component of seismic and GPS data.

In order to investigate the effect of the choice of rupture velocity on the inversion result, we test the inversion of the synthetic data (produced with a rupture velocity of 4.2 km s^{-1}) with rupture velocities from 2.0 to 5.0 km s^{-1}. We find that the VR drops to 70.5 per cent for the low (2.6 km s^{-1}) rupture velocity that is generally obtained for other earthquakes in central Taiwan (e.g. Ji *et al.* 2003; Chi & Dreger 2004). It is also notable that the inversion cannot resolve the deeper portion of the slip distribution given a much slower rupture velocity, and the depth of the slip asperities changes as rupture velocities are varied (see the different rupture velocities in Fig. 15). However, no matter the variation of the rupture velocity, the variance reduction does not change much for the synthetic GPS or InSAR data sets (all above 96 per cent for all rupture velocities). This suggests that the geodetic data are not very sensitive to the details of the slip distribution at greater depths, and therefore the temporal constraint on the earthquake source from the seismic data is very important to resolve the slip distribution on the fault plane.

6 DISCUSSION

6.1 Comparison with other studies

The geodetic and joint inversions show the total moment of the Jia-Shian event as 3.30×10^{18} and 3.25×10^{18} N m, which both equal M_w 6.34. Fig. 11 shows the inversion results of the geodetic and the joint inversions. The coloured circles represent the aftershocks in the first 24 hours following the mainshock (Huang *et al.* 2011). From this figure, the main difference between the geodetic and the joint inversions is the slip area. The main slip area of the joint inversion is more compact and surrounded by the aftershocks, whereas the slip area of the geodetic inversion is observed inside and outside of the aftershocks (e.g. the smaller slip asperity on the left-hand side of the epicentre in Fig. 11a). The difference might be due to additional postseismic displacement that may be observed by the GPS and InSAR data. As a result, the geodetic inversion would also include some afterslip, whereas the joint inversion has weighting from seismic data and would be more restricted to the mainshock. Thus, the joint inversion better represents the coseismic slip distribution due to the mainshock. We can clearly see that most of the aftershocks are located along the upper peripheries of both inversions, which indicates that the aftershocks lie along the

Downloaded from http://gji.oxfordjournals.org/ at University of California, Berkeley on August 15, 2013

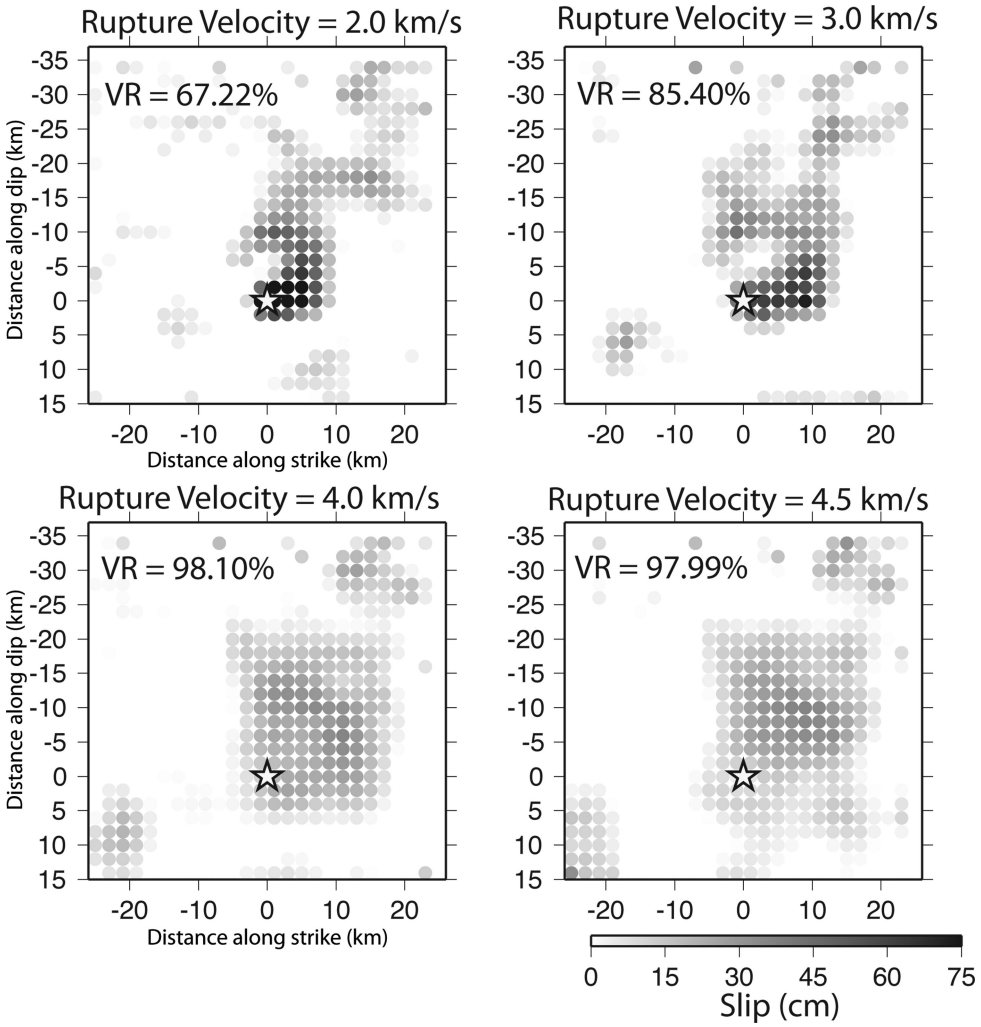

Figure 15. Joint inversion using synthetic input from forward model shown in Fig. 14(e). The forward model has a rupture velocity of 4.2 km s^{-1} and inversions are tested with a range of rupture velocities. Note that even though the incorrect rupture velocity can significantly decrease the fit to the seismic data, it does not significantly change the fit to the geodetic data (VR of the geodetic data are above 96 per cent for all models shown).

highly stressed coseismic slip margin. Both the slip area and the aftershock distribution indicate that the main slip asperity is about 226 km^2 with about 43 cm peak slip obtained in the joint inversion. The difference in total moment between the geodetic and the joint inversions is about 5×10^{16} N m, which is equivalent to a M_w 5.1 earthquake. Since the largest aftershock of this event is M_w 5.0 (3.54×10^{16} N m) that occurred about 8 hours later, the difference between the geodetic and joint inversions could largely be due to this and other aftershocks.

Similar work has been done by Ching *et al.* (2011) (GPS inversion), Hsu *et al.* (2011) (GPS inversion), and Lee *et al.* (2012) (seismic and GPS combined inversion). Both Ching *et al.* (2011) and Hsu *et al.* (2011) inferred about 12 cm peak coseismic slip, whereas Lee *et al.* (2012) found 35 cm. The total moment obtained in previous studies differs, but is of the same order (2.92×10^{18} from Ching *et al.*; 4.95×10^{18} from Hsu *et al.*; 6.53×10^{18} from Lee *et al.* units in N m). The GPS data we use are the same as Hsu *et al.* (2011) and similar to the data used by Ching *et al.* (2011) and Lee *et al.* (2011), so the main differences could be the result of different model parameterizations (subfault discretization and smoothing), or the velocity structure applied (half-space geodetic inversion for Ching *et al.* 2011 and Hsu *et al.* 2011; CWB 1-D velocity for Lee *et al.* 2012; two refined 1-D velocity structures represented for west- and east-Taiwan for seismic inversion and layered model for geodetic inversion in this study).

Mai & Beroza (2000) develop source-scaling properties based on finite-source rupture models. They estimate the empirical relations between the seismic moment and fault length, fault width, and mean slip for dip-slip and strike-slip events. According to their empirical relations, a $M_o = 3.25 \times 10^{18}$ N m event would have a fault area = 105 km^2 with length = 10.8 km and width = 9.7 km and mean slip = 104.7 cm. Our joint inversion result suggests a fault area = 286 km^2 and mean slip ≈20 cm. In other word, the slip area of Jia-Shian event is 2.7 times larger than the average, and the mean slip is only 1/5 of that expected for a M_w 6.3 event. Nevertheless, while the values of fault length, width and mean slip of Jia-Shian deviate from the average, they are still within the standard errors (i.e. the *a* and *b* values in Mai & Beroza 2000). This lower mean slip value also suggests that the Jia-Shian event was a low stress-drop event. Given the mean slip of 15 cm on a 20 km × 25 km main asperity (Fig. 11b), the static stress drop of the Jia-Shian event is 0.24 MPa. This value of stress drop is at least ten times smaller than the 1999 Chi-Chi earthquake (6.5 or 22.5 MPa, Huang *et al.* 2001; Ma *et al.* 2001) and its aftershocks (Chi & Dreger 2004), and in the low range of

Downloaded from http://gji.oxfordjournals.org/ at University of California, Berkeley on A 13

global average stress drops for reverse events (Mai & Beroza 2000; Allmann & Shearer 2009).

6.2 The relation with the CTFZ and regional seismicity

The NW–SE strike-slip CTFZ was proposed by Deffontaines *et al.* (1997) based on morphological evidence and field mapping (Fig. 1a). Mapped shear bands in the surrounding mudstones in this region indicate a left-lateral sense of shear that has a minimum $12 \pm 4\,\mathrm{mm\,yr^{-1}}$ slip-rate based on offset geologic markers and sparse GPS data (Deffontaines *et al.* 1997). Ching *et al.* (2011) argued that based on this long-term slip rate and the coseismic peak slip of about 19 cm from their geodetic inversion, an earthquake with a magnitude similar to the Jia-Shian event would occur every 12–24 years. This rapid recurrence rate is inconsistent with the observed low strain rate and low background seismicity in the source area (Ching *et al.* 2011), it assumes that all CTFZ displacement is accommodated by the fault on which the Jia-Shian event occurred, and the slip rate on the fault plane at 20 km deep is unknown. In addition, the peak coseismic slip is quite uncertain and depends on the smoothing and rupture velocity applied to the inversion, as we showed in the synthetic tests.

A recent study by Rau *et al.* (2012) indicates that the NW-trending Jia-Shian earthquake sequence and the upward extension of the rupture to the surface correspond to the CTFZ. However, based on the result of our individual and joint inversions (Fig. 6), there is a minor slip asperity in the western shallower part of the fault. The surface projection of this minor patch coincides with the *Lungchuan anticline* (location see Fig. 9a), which is about 13 km south of the CTFZ. Hence, the Jia-Shian fault plane does not extend to the inferred CTFZ unless the dip changes with depth on the fault (Ching *et al.* 2011).

The Jia-Shian earthquake occurred in a transition zone separating regions of distinctly different depth extent of seismicity and seismic velocity. A S-to-N profile of the regional seismicity and *Vp* tomography (seismicity and velocity tomography data from Wu *et al.* 2007, 2009) of SW Taiwan is shown in Fig. 16. The seismicity data clearly show a change in depth to the base of the seismogenic zone from about 15 km in the north to about 25 km in the south, near latitude 22.8°–23°N. A corresponding change is observed in tomographic *Vp* velocity models, with a 5-km-thick near-surface low velocity layer ($Vp < 4.5\,\mathrm{km\,s^{-1}}$) in the north increasing to about 10 km depth in the south. There is an apparent gap in seismicity at 22.9°N that seems to be filled by the Jia-Shian mainshock and aftershocks (Figs 1 and 16). However, the north dipping Jia-Shian earthquake clearly did not involve faulting parallel to this south dipping seismicity transition zone. Nevertheless, both the Jia-Shian event and the transition zone represent ESE–WNW striking structures in SW Taiwan that may correspond to Miocene structures formed during the extension of the south China Sea (Teng 1990) and were reactivated during the latest orogeny. The change in crustal strain orientations across this area described in the next section may also relate to the effect of such deep-seated pre-existing structures.

6.3 Paleostress analysis and crustal scale strain

Lacombe *et al.* (1999) analyse the paleostress inferred from regional fault orientations and slip vectors and find two Quaternary stress regimes: an early period of NW–SE (~140°) compression followed by more recent E–W (080°) compression (Fig. 17). The earlier direction of compression appears to reflect the current direction of plate convergence, whereas the second direction prevailed only in the latest stage of folding. Recently, a study by Huang *et al.* (2010) on the paleostress orientations near Laonungshi to the north of the Jia-Shian earthquake (location see Figs 1b and 17c) resolved two primary NW–SE and WNW–ESE, and one NE–SW compressional directions. The NE–SW compression represents the youngest stage based on cross-cutting relationships, but the age is not well constrained. While the orientation of inferred stress axes in SW Taiwan is quite heterogeneous (Fig. 17c), the paleostress studies provide some evidence for recent initiation of an E–W compressional stress regime near the Jia-Shian earthquake.

Geodetic measurements can be used to determine interseismic strain rate fields and the orientation of the principal strain axes across Taiwan. We consider GPS measurements of the horizontal strain rate tensor and the orientation and rate of regional horizontal principal

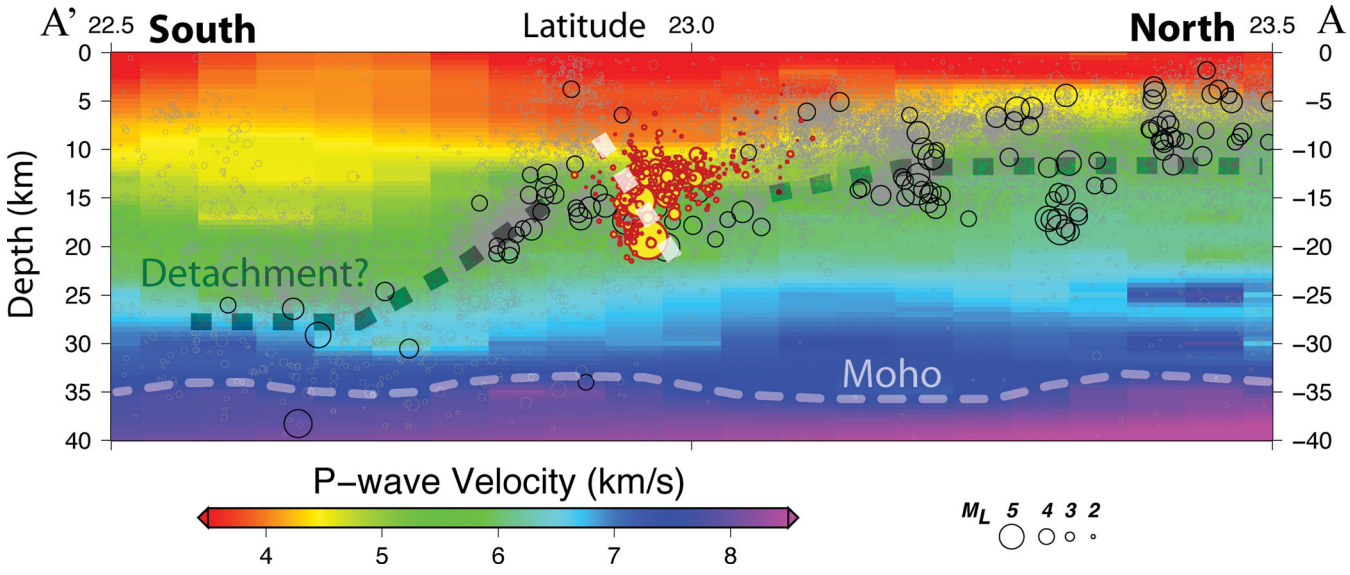

Figure 16. Distribution of seismicity from 1991 to 2009 (data from Wu *et al.* 2009) along S-to-N profile AA′ in Fig. 1(a). The grey circles are the seismicity lower than M_w 4.0; the black circles are those larger than M_w 4.0. The red circles show the Jia-Shian main shock and its aftershocks (Huang *et al.* 2011). The background colours show the regional *P*-wave tomography model of Wu *et al.* (2007) along the same profile.

Downloaded from http://gji.oxfordjournals.org/ at University of California, Berkeley on August 15, 2013

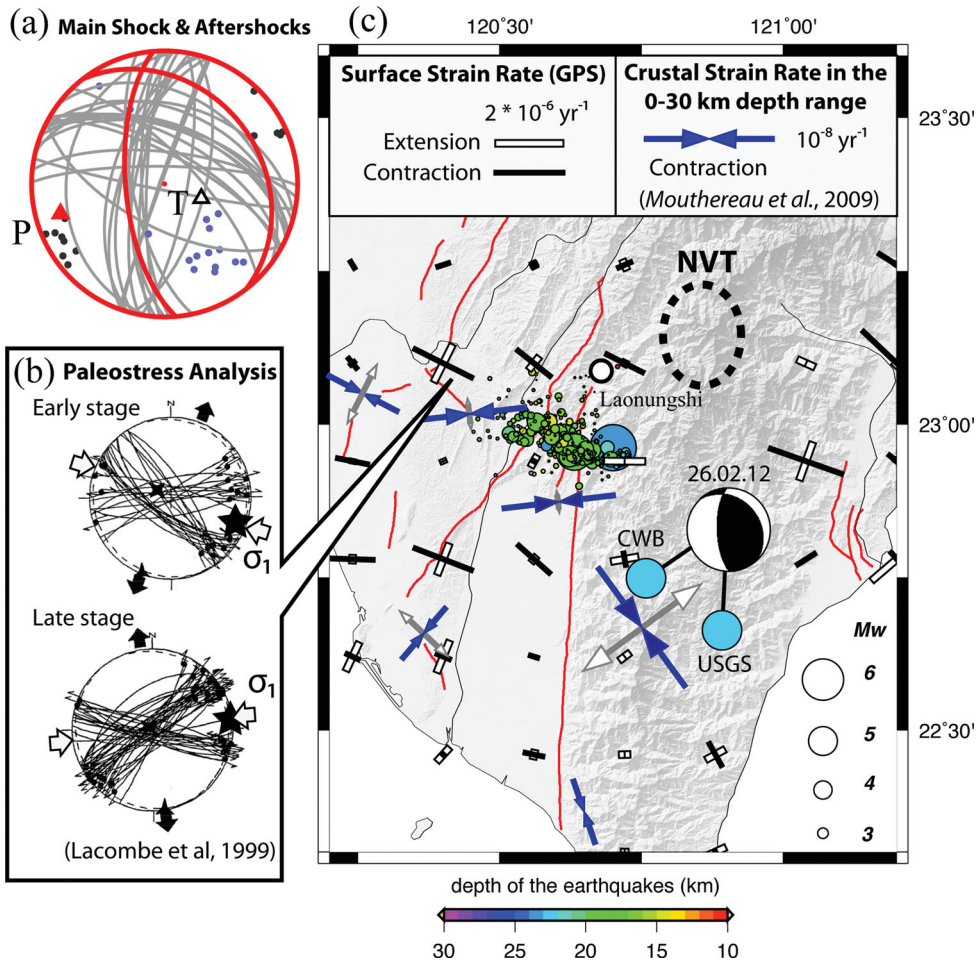

Figure 17. (a) Focal mechanisms of the Jia-Shian main shock (red) and its aftershocks (grey). The red and white triangles represent the *P*- and *T*-axes of the main shock; the black and blue dots represent the *P*- and *T*-axes of the aftershocks. (b) Paleostress reconstruction based on fault slip analysis of the CTFZ in SW Taiwan (after Lacombe *et al.* 1999). (c) Surface (bars) and crustal (arrows) two-dimensional strain rate tensor measurements in SW Taiwan obtained from GPS and seismicity data, respectively. A cluster of NVT identified by Chao *et al.* (2012) is outlined with dashed ellipse. The beach ball diagram shows the 2012 February 26, event and its epicentre located by CWB and USGS.

strains inferred from earthquake focal mechanisms. The surface strain rate estimated by GPS measurements between 2000 and 2005 (Fig. S6, GPS data from Kuo 2008) indicates E–W to SE–NW directed contraction in SW Taiwan. The orientation of maximum shortening is close to the current direction of plate collision (Lin *et al.* 2010). In the area of the Jia-Shian event, there seems to be a transition from shortening to extension between the Western Foothills and the Central Range. This is in contrast to the strain field based on focal mechanism inversions (dark blue arrows in Fig. 17; after Mouthereau *et al.* 2009), which shows ENE–WSW contraction in the northern Pingtung plain and the Western Foothill near the Jia-Shian event, but SE–NW oriented contraction in the southern Central Range. This ENE–WSW shortening has the same orientation as the *P* axis of the mainshock (this study) and most of the aftershocks (Huang *et al.* 2011). Thus, the major compression axis of the Jia-Shian event agrees with the ambient strain distribution at source depth (21 km) but not the geodetic strain field observed at the surface.

6.4 Latest aftershock and nearby tremors

In 2012 February 26, an M_w 5.7 earthquake occurred about 25 km (USGS solution) or 40 km (CWB location) southeast of the Jia-Shian sequence (Fig. 17). Both the focal mechanism and the source depth (22.5 km) of this earthquake are similar to the Jia-Shian mainshock. This recent earthquake can be considered as an aftershock of the Jia-Shian event due to the similar focal mechanism and source depth, and may have involved slip on the same geological structure. The appearance of this recent event may indicate that this NW–SE structure (Fig. 1a) extends further to the southeast beneath the Central Range of Taiwan, but whether or not this represents a SE continuation of the CTFZ is unclear.

A recent study of non-volcanic tremor (NVT) by Chao *et al.* (2012) finds deep triggered tremors located beneath the Central Range at 15–25 km depth, about 20 km north of the Jia-Shian sequence. The tremors were triggered by several M_w 7.5+ earthquakes at distances of more than 1000 km. These triggered tremors are bursts of high frequency (2–8 Hz), non-impulsive and long-duration seismic energy modulated by surface waves. Chao *et al.* (2012) explain the triggered tremors as Coulomb failure involving NS-striking, left-lateral shear on a low-angle detachment fault at the base of the seismogenic zone of the Central Range, but the steeply E-dipping Chaochou-Lishan Fault has also been suggested as a possible source structure of tremor activity in S Taiwan (Tang *et al.* 2010). It may be worth exploring the triggering potential of deep-seated receiver faults with a Jia-Shian type orientation. The

Downloaded from http://gji.oxfordjournals.org/ at University of California, Berkeley on A 13

repeated teleseismic triggering of tremor suggests the existence of weak fault structures in the lower crust below the Central Range and SW Taiwan. Future studies of this tremor activity may improve our understanding of the deep roots of the deformation zone associated with the Jia-Shian earthquake.

6.5 Thick or thin skinned model

The depth of the nucleation of this event seems to support a thick-skinned model for SW Taiwan (Ching *et al.* 2011), even though there is some inconsistency in the depth between the previous studies (e.g. 23 km from CWB, 23–24 km from Ching *et al.* 2011 and Huang *et al.* 2011) and our finite source inversion (18–19 km). The earthquake occurred within a NW–SE oriented transition zone across which the depth to the base of seismicity increases by about 10 km to the south, possibly associated with the CTFZ proposed by Deffontaines *et al.* (1997). The latest M_w 5.7 aftershock implies that this NW–SE structure may extend at least 50 km into the south Central Range. This structure may also involve pre-existing normal faults that are associated with the opening of the South China Sea during Miocene pre-collision stage (Lin & Watts 2002; Rau *et al.* 2012). However, the actual geometry of these preexisting structures and their relationship with the CTFZ, the source fault of the Jia-Shian earthquake, the orientation of active shortening, and the topographic expression of the active tectonics in this area are not well understood. Hence, models considering more complex fault geometry, and an improved velocity structure model may be needed to gain further insight about the structure and setting of the Jia-Shian event, and provide more information on this long lasting debate.

7 CONCLUSION

In this study we apply finite source inversion techniques relying on seismic, GPS and InSAR data individually, as well as in a joint inversion to obtain rupture models of the 2010 Jia-Shian earthquake. Contrary to previous studies of this event, we generate separate Green's functions for seismic stations in west and east Taiwan by fitting the waveforms of the largest aftershock to calibrate the velocity structure and Green's functions. We also find the proper frequency band for fitting the largest aftershock to apply for the inversion of mainshock data for finite-source parameters. In addition, we use a layered elastic model for the geodetic inversions to help with obtaining a more reliable slip distribution. These efforts result in high consistency between the models obtained independently from the different data sets. A comprehensive test of the model smoothing of each data set and the weighting between different data sets for the joint inversion represents an objective way to investigate the model parameters and solutions, and to find the best weighting relation between the different data sets. The station sensitivity test done by the random removal of 20 per cent data shows the main features of the inversion result are stable. The resolution test with added noise also informs on the confidence of the shallower slip, and the effect of the smoothing we applied on the solution. The individual inversions using seismic or geodetic data show consistent peak slip, slip area, and magnitude of the Jia-Shian mainshock. The total moment of this event obtained in the joint inversion is 3.25×10^{18} N m, which is equivalent to an M_w 6.3 event. Rupture velocity tests suggest that this event was a supershear event propagating at about 1.23 of the regional shear-wave velocity.

The Jia-Shian event in SW Taiwan occurred along the boundary between the western Foothills and the Central Range to the north and east and the sedimentary Pingtung Basin in the south. This boundary coincides with a transition zone from shallower (north) to deeper (south) seismicity and the previously proposed CTFZ at the surface. However, since the up-dip extension of the coseismic slip is located south of the CTFZ, whether or not the Jia-Shian event is within the CTFZ at depth remains unclear. The youngest paleostress orientations and compression axes from seismic data are consistent with the kinematics of the Jia-Shian earthquake. Around the region of the Jia-Shian sequence, the stress orientation in the upper crust inferred from focal mechanism data is not consistent with the directions of the surface strain rate field derived from GPS or the current plate collision. The location of the most recent large aftershock (M_w 5.7) reveals that the deep structure extends further to the SE below the Central Range. Consequently, the Jia-Shian event may represent the reactivation of pre-existing deep structures, and the orientation of stress locally deviates from the current orientation of plate collision.

ACKNOWLEDGEMENTS

We thank Ya-Ju Hsu for providing the coseismic GPS data; Wen-Thong Liang and Wu-Cheng Chi for providing the strong motion data; Yih-Min Wu for providing the Taiwan regional tomography data; Hsin-Hua Huang for providing the aftershocks relocation catalog. The GPS and seismic data including strong motion and broadband stations (BATS) are deployed and collected by IES, Academia Sinica of Taiwan and CWB, Taiwan. Special thanks to Yih-Min Wu, Chung Huang, John Suppe, Sierra Boyd, Hsin-Hua Huang, Lung-Cheng Kuo, Ya-Ju Hsu and Jyr-Ching Hu for discussions and ideas that greatly benefitted this research. We would like to thank two anonymous reviewers for the constructive review of the manuscript. This project is supported by the National Science Foundation grant (EAR 0738298). Most of the figures are made with GMT (Wessel & Smith 1995). This is Berkeley Seismological Laboratory contribution #12–18.

REFERENCES

Allmann, B.P. & Shearer, P.M., 2009. Global variations of stress drop for moderate to large earthquake, *J. geophys. Res.,* **114,** B01310, doi:10.1029/2008JB005821.

Bouchon, M. & Vallée, M., 2003. Observation of long supershear rupture during the magnitude 8.1 Kunlunshan earthquake, *Science,* **301,** 824–826.

Chao, K., Peng, Z., Wu, C., Tang, C.-C. & Lin, C.-H., 2012. Remote triggering of non-volcanic tremor around Taiwan, *Geophys. J. Int.,* **188,** 301–324.

Chi, W.-C. & Dreger, D., 2002. Finite fault inversion of the September 25, 1999 (Mw = 6.4) Taiwan earthquake: implications for GPS displacements of Chi-Chi, Taiwan earthquake sequence, *Geophys. Res. Lett.,* **29,** 1694, doi:10.1029/2002GL015237.

Chi, W.-C. & Dreger, D., 2004. Crustal deformation in Taiwan: results from finite source inversions of six Mw > 5.8 Chi-Chi aftershocks, *J. geophys. Res.,* **109,** B07305, doi:10.1029/2003JB002606.

Ching, K.-E., Johnson, K.M., Rau, R.-J., Chuang, R.Y., Kuo, L.-C. & Leu, P.-L., 2011. Inferred fault geometry and slip distribution of the 2010 Jiashian, Taiwan, earthquake is consistent with a thick-skinned deformation model, *Earth planet. Sci. Lett.,* doi:10.1016/j.epsl.2010.10.021.

Cohee, B.P. & Beroza, G.C., 1994. Slip distribution of the 1992 Landers Earthquake and Its Implications for Earthquake Source Mechanics, *Bull. seism. Soc. Am.,* **84,** 692–712.

Deffontaines, B. *et al.*, 1997. Quaternary transfer faulting in the Taiwan Foothills: evidence from a multisource approach, *Tectonophysics,* **274,** 61–82.

Downloaded from http://gji.oxfordjournals.org/ at University of California, Berkeley on August 15, 2013

Dreger, D. & Kaverina, A., 2000. Seismic remote sensing for the earthquake source process and near-source strong shaking: a case study of the October 16, 1999 Hector Mine earthquake, *Geophys. Res. Lett.,* **27,** 1941–1944.

Dunham, E.M., 2007. Conditions governing the occurrence of supershear ruptures under slip-weakening friction, *J. geophys. Res.,* **112,** B07302, doi:10.1029/2006JB004717.

Dunham, E.M. & Archuleta, R.J., 2004. Evidence for a supershear transient during the 2002 Denali fault earthquake, *Bull. seism. Soc. Am.,* **94**(6B), S256–S268.

Ellsworth, W.L. *et al.*, 2004. Near-field ground motion of the 2002 Denali fault, Alaska, earthquake recorded at pump station 10, *Earthquake Spectra,* **20,** 597–615.

Hartzell, S.H. & Heaton, T.H., 1983. Inversion of strong ground motion and teleseismic waveform data for the fault rupture history of the 1979 Imperial Valley, California, earthquake, *Bull. seism. Soc. Am.,* **73,** 1553–1583.

Hsu, Y.-J., Yu, S.-B., Kuo, L.-C., Tsai, Y.-C. & Chen, H.-Y., 2011. Coseismic deformation of the 2010 Jiashian, Taiwan earthquake and implications for fault activities in southwestern Taiwan, *Tectonophysics,* **502,** 328–335.

Hu, J.-C. *et al.*, 2007. Fault activity and lateral extrusion inferred from velocity field revealed by GPS measurements in the Pingtung area of southwestern Taiwan, *J. Asian Earth Sci.,* **31,** 287–302.

Huang, C., Byrne, T. & Mirakian, D., 2010. Geologic Setting of the 2010 Jiasian earthquake, southern Taiwan, Abstract T23D-03 presented at 2010 Fall Meeting, AGU, San Francisco, California, December 13–17.

Huang, H.-H., Wu, Y.-M., Lin, T.-L., Chao, W.-A., Shyu, J.B.H., Chan, C.-H. & Chang, C.-H., 2011. The preliminary Study of the 2010 Mw 6.3 Jiasian, Taiwan, Earthquake Sequence, *Terr. Atmos. Ocean. Sci.,* **22**(3), 283–290.

Huang, W.-G., Wang, J.-H., Huang, B.-S., Chen, K.-C., Chang, T.-M., Hwang, R.-D., Chiu, H.-C. & Tsai, C.-C.P., 2001. Estimates of Source Parameters for the 1999 Chi-Chi, Taiwan, Earthquake Based on Brune's Source Model, *Bull. seism. Soc. Am.,* **91**(5), 1190–1198.

Ji, C., Helmberger, D. V., Wald, D. J. & Ma, K.-F., 2003. Slip history and dynamic implications of the 1999 Chi-Chi, Taiwan, earthquake, *J. Geophys. Res.* **108,** B9, 2412, doi:10.1029/2002JB001764.

Kaverina, A., Dreger, D. & Price, E., 2002. The Combined Inversion of Seismic and Geodetic Data for the Source Process of the 16 October 1999 Mw 7.1 Hector Mine, California, Earthquake, *Bull. Seism. Soc. Am.* **92 (4),** 1266–1280.

Kim, A. & Dreger, D.S., 2008. Rupture process of the 2004 Parkfield earthquake from near-fault siesmic waveform and geodetic records, *J. geophys. Res.,* **113,** B07308, doi:10.1029/2007JB005115.

Kuo, S.-M., 2008. Earthquake potential of SW Taiwan inferred from GPS and seismic data, *Master thesis,* National Cheng Kung University, pp. 66.

Lacombe, O., Mouthereau, F., Deffontaines, B., Angelier, J., Chu, H.-T. & Lee, C.-T., 1999. Geometry and Quaternary kinematics of fold-and-thrust units of southwestern Taiwan, *Tectonics,* **18,** 1198–1223.

Lacombe, O., Mouthereau, F., Angelier, J. & Deffontaines, B., 2001. Structural, geodetic and seismological evidence for tectonic escape in SW Taiwan, *Tectonophysics,* **333,** 323–345.

Lee, S.-J., Mozziconacci, L., Liang, W.-T., Hsu, Y.-J., Huang, W.-G. & Huang, B.-S., 2011. Source complexity of the 4 March 2010 Jiashian, Taiwan, Earthquake determined by joint inversion of teleseismic and near field data, *J. Asian Earth Sci.,* doi:10.1016/j.jseaes.2012.11.018.

Lin, A.-T. & Watts, A.B., 2002. Origin of the West Taiwan basin by orogenic loading and flexure of a rifted continental margin, *J. geophys. Res.,* **107**(B9), 2185, doi:10.1029/2001JB000669.

Lin, K.-C. *et al.*, 2010. GPS crustal deformation, strain rate, and seismic activity after the 1999 Chi-Chi earthquake in Taiwan, *J. geophys. Res.,* **115,** B07404, doi:10.1029/2009JB006417.

Ma, K.-F., Mori, J., Lee, S.-H. & Yu, S.-B., 2001. Spatial and temporal distribution of slip for the 1999 Chi-Chi, Taiwan, Earthquake, *Bull. seism. Soc. Am.,* **91**(5), 1069–1087.

Mai, P.M. & Beroza, G.C., 2000. Source scaling properties from finite-fault-rupture models, *Bull. seism. Soc. Am.,* **90,** 604–615.

Minson, S.E. & Dreger, D.S., 2008. Stable inversions for complete moment tensors, *Geophys. J. Int.,* **174,** 585–592, doi:10.1111/j.1365-246X.2008.03797.x.

Mouthereau, F., Fillon, C. & Ma, K.-F., 2009. Distribution of strain rates in the Taiwan orogenic wedge, *Earth planet. Sci. Lett.,* **284,** 361–385.

Pasyanos, M.E., Dreger, D.S. & Romanowicz, B., 1996. Toward real-time estimation of regional moment tensors, *Bull. seism. Soc. Am.,* **86**(5), 1255–1269.

Rau, R.-J., Lee, J.-C., Ching, K.-E., Lee, Y.-H., Byrne, T.B. & Chen, R.-Y., 2012. Subduction-continent collision in southwestern Taiwan and the 2010 Jiashian earthquake sequence, *Tectonophysics,* **578,** 107–116, doi:10.1016/j.tecto.2011.09.013.

Rosen, P.A., Hensley, S. & Peltzer, G., 2004. Updated Repeat Orbit Interferometry Package Released, *EOS, Trans. Am. geophys. Un.,* **85**(5), 35.

Saikia, C.K., 1994. Modified frequency-wave-number algorihm for regional seismograms using Filon's quadrature-modeling of L(g) waves in eastern North America, *Geophys. J. Int.,* **118,** 142–158.

Shin, C., Yoon, K., Marfurt, K.J., Park, K., Yang, D., Lim, H.Y., Chung, S. & Shin, S., 2001. Efficient calculation of a partial-derivative wavefield using reciprocity for seismic imaging and inversion, *Geophysics,* **66,** 1856–1863.

Somerville, P.G. *et al.*, 1999. Characterizing crustal earthquake slip models for the prediction of strong ground motion, *Seismo. Res. Lett.,* **70,** 59–80.

Suppe, J., 1981. Mechanics of mountain building and metamorphism in Taiwan, *Mem. geol. Soc. China,* **4,** 67–89.

Tarantola, A., 2005. Inverse Problem Theory and Model Parameter Estimation, Society for Industrial and Applied Mathematics, Philadelphia.

Tang, C.-C., Peng, Z., Chao, K. & Lin, C.-H., 2010. Detecting low-frequency earthquakes within non-volcanic tremor in southern Taiwan triggered by the 2005 Mw 8.6 Nias earthquake, *Geophys. Res. Lett.,* **37,** L16307, doi:10.1029/2010GL043918.

Teng, L., 1990. Geotectonic evolution of late Cenozoic arc-continent collision in Taiwan, *Tectonophysics,* **183,** 57–76.

Wald, D.J. & Somerville, P.G., 1995. Variable-slip rupture model of the great 1923 Kanto, Japan earthquake: geodetic and body-waveform analysis, *Bull. seism. Soc. Am.,* **85,** 159–177.

Wald, D.J. & Heaton, T.H., 1994. Spatial and temporal distribution of slip for the 1992 Landers, California earthquake, *Bull. seism. Soc. Am.,* **84,** 668–691.

Wald, D.J., Heaton, T.H. & Hudnut, K.W., 1996. Rupture history of the 1994 Northridge, California earthquake from strong-motion, GPS, and leveling data, *Bull. seism. Soc. Am.,* **86,** S49–S70.

Walker, K. T. & Shearer, P. M., 2009. Illuminating the near-sonic rupture velocities of the intracontinental Kokoxili Mw 7.8 and Denali fault Mw 7.9 strike-slip earthquakes with global P wave back projection imaging, *J. Geophys. Res.,* **114.** B02304, doi:10.1029/2008JB005738.

Wang, C.Y. & Herrmann, R.B., 1980. A numerical study of P-, SV-, and SH-wave generation in a plane layered medium, *Bull. seism. Soc. Am.,* **70**(4), 1015–1036.

Wang, R., Martin, F. & Roth, F., 2003. Computation of deformation induced by earthquakes in multi-layered elastic crust: FORTRAN programs EDGRN/EDCMP, *Comput. Geosci.,* **29,** 195–207.

Wessel, P. & Smith, W.H.F., 1995. New version of the generic mapping tools released, *EOS, Trans. Am. geophys. Un.,* **76**(29), 329.

Wu, F.T., Rau, R.J. & Salzberg, D.H., 1997. Taiwan orogeny: thin-skinned or lithospheric collision? *Earth planet. Sci. Lett.,* **133,** 517–532.

Wu, Y.-M., Chang, C.-H., Zhao, L., Shyu, J.B.H., Chen, Y.-G., Sieh, K. & Avouac, J.P., 2007. Seismic tomography of Taiwan: improved constraints from a dense network of strong-motion station, *J. geophys. Res.,* **112,** B08312, doi:10.1029/2007JB004983.

Wu, Y.-M., Shyu, J.B.H., Chang, C.H., Zhao, L., Nakamura, M. & Hsu, S.-K., 2009. Improved seismic tomography offshore northeastern Taiwan: implications for subduction and collision processes between Taiwan and the southernmost Ryukyu, *Geophys. J. Int.,* **178,** 1042–1054.

Yoo, S.-H., Rhie, J., Choi, H. & Mayeda, K., 2010. Evidence for non-self-similarity and transitional increment of scaled energy in the 2005 west off Fukuoka seismic sequence, *J. geophys. Res.,* **115,** B08308, doi:10.1029/2009JB007169.

Downloaded from http://gji.oxfordjournals.org/ at University of California, Berkeley on A 13

Yoshida, S. & Koketsu, K., 1990. Simultaneous inversion of wave-form and geodetic data for the rupture process of the 1984 Naganoken Seibu, Japan, earthquake, *Geophys. J. Int.,* **103,** 355–362, doi:10.1111/j.1365-246X.1990.tb01776.x.

Yu, S.-B., Chen, H.-Y. & Kuo, L.-C., 1997. Velocity field of GPS stations in the Taiwan area, *Teconophysics,* **274,** 41–59, doi:10.1016/S0040-1951(96)00297-1.

Yu, S.-B., Hsu, Y.-J., Kuo, L.-C., Chen, H.-Y. & Liu, C.-C., 2003. GPS measurement of postseismic deformation following the 1999 Chi-Chi, Taiwan, earthquake, *J. geophys. Res.,* **108,** doi:10.1029/2003JB002396.

SUPPORTING INFORMATION

Additional Supporting Information may be found in the online version of this paper:

Figure S1. The comparison of synthetic (red) and the data (black) by using joint inversion. CHY102, CHY074, KAU049, TTN026, TTN051, TTN052 and TTN053 are strong motion stations. YULB, SSLB and MASB are broadband stations. All of the waveforms are bandpassed to 0.03–0.3 Hz. The locations of all stations see in Fig. 1(b).

Figure S2. The predicted GPS displacement based on joint inversion and the residual. (a) The black and white arrows represent the data and predictions of horizontal motions, respectively. The rectangular grids represent the coseismic slip projected onto the surface. (b) The colour and size of the circle represents the GPS vertical coseismic displacement. The circles without outlines and the circles with black outlines are the data and predictions, respectively. (c) The arrows and colours in the circles are the residuals between the GPS data and predictions.

Figure S3. The predicted InSAR displacement based on joint inversion and the residual. (a) Coseismic InSAR measurements after downsampling and noise reduction (see text). The spatial resolution is about one pixel per km^2. (b) InSAR prediction with the same colour scale. (c) Difference between the observed and predicted InSAR observations. The orange star represents the epicentre of the earthquake, and the grey dashed lines represent the fault model.

Figure S4. Joint inversion with different rupture velocities. Rupture velocity $= 3.0\,km\,s^{-1}$ is equivalent to the Rayleigh velocity in this region.

Figure S5. Synthetic resolution tests with seismic only inversion.

Figure S6. (a) Surface strain rate from 2002 to 2007 (GPS data from Kuo 2008). (b) Strain change obtained from GPS station offsets due to the Jia-Shian earthquake. (http://gji.oxfordjournals.org/lookup/supp1/doi:10.1093/gji/ggt058/-/DC1)

Please note: Oxford University Press are not responsible for the content or functionality of any supporting materials supplied by the authors. Any queries (other than missing material) should be directed to the corresponding author for the paper.

Downloaded from http://gji.oxfordjournals.org/ at University of California, Berkeley on August 15, 2013